Transition of the Hurricane Boundary Layer During the Landfall of Hurricane Irene (2011)

A. Addison Alford[1], Jun A. Zhang[2,3], Michael I. Biggerstaff[1,4,5], Peter Dodge[2], Frank D. Marks[2], and David J. Bodine[4]

[1]School of Meteorology, University of Oklahoma, Norman, OK

[2]Hurricane Research Division, NOAA Atlantic Oceanographic and Meteorological Laboratory, Miami, FL

[3]Cooperative Institute for Marine and Atmospheric Studies, University of Miami, Miami, FL

[4]Advanced Radar Research Center, University of Oklahoma, Norman, OK

[5]Cooperative Institute for Mesoscale Meteorological Studies, University of Oklahoma, Norman, OK

Submitted to the Journal of the Atmospheric Sciences

Corresponding author: Dr. Michael I. Biggerstaff, National Weather Center, Suite 5900, 120 David L. Boren Blvd, Norman, OK 73019

Email: drdoppler@ou.edu

Abstract

The hurricane boundary layer (HBL) has been observed in great detail through aircraft investigations of tropical cyclones over the open ocean, but the coastal transition of the HBL has been less frequently observed. During the landfall of Hurricane Irene (2011), research and operational aircraft over water sampled the open ocean HBL simultaneously with ground-based research and operational Doppler radars onshore. The location of the radars afforded 13 hours of dual-Doppler analysis over the coastal region. Thus, the HBL from the coastal waterways, through the coastal transition, and onshore was observed in great detail for the first time. Three regimes of HBL structure were found. The outer bands were characterized by temporal perturbations of the HBL structure with attendant low-level wind maxima in the vicinity of rainbands. The inner core, in contrast, did not produce such perturbations, but did see a reduction of the height of the maximum wind and a more jet-like HBL wind profile. In the eyewall, a tangential wind maximum was observed within the HBL over water as in past studies and above the HBL onshore. However, the transition of the tangential wind maximum through the coastal transition showed that the maximum continued to reside in the HBL through 5 km inland, which has not been observed previously. It is shown that the adjustment of the HBL to the coastal surface roughness discontinuity does not immediately mix out the residual high momentum jet aloft. Thus, communities closest to the coast are likely to experience the strongest winds onshore prior to the complete adjustment of the HBL.

1. Introduction

Understanding the distribution of winds, intensity change, and tropical cyclone (TC) structure requires comprehensive knowledge of the storm's atmospheric boundary layer

45 (hereafter referred to as the Hurricane Boundary Layer [HBL]; e.g., Montgomery et al. 2014).
46 The structure of the HBL can influence the vertical distribution of momentum through turbulent
47 fluxes, which in turn can influence the horizontal distribution of the maximum wind experienced
48 at any one location, particularly during landfall (Wurman and Winslow 1998; Alford et al. 2019).
49 Due to the increase in aerodynamic surface roughness over land versus that over the open ocean,
50 sustained wind speeds are expected to decrease while the dynamic boundary layer is expected to
51 increase in depth (Elliott 1958; Garratt 1990; Tang and Tan 2006; Hirth et al. 2012; Williams
52 2019).

53 Observations of the mean HBL structure over the open ocean are generally plentiful
54 (Wang et al. 2015; Zhang et al. 2011). High vertical resolution (10-20 m) dropsonde (Hock and
55 Franklin 1999) observations have been collected by several airborne platforms including the
56 National Oceanic and Atmospheric Administration's (NOAA's) WP-3D Orion and G-IV jet
57 (Aberson et al. 2006) operated by the NOAA Aircraft Operations Center, the C-130 Hurricane
58 Hunter aircraft operated by the United States Air Force (USAF; e.g., Franklin et al. 2003), the
59 HIAPER aircraft operated by National Science Foundation (NSF; UCAR/NCAR 2005), and the
60 DC-8 and Global Hawk operated by the National Aeronautics and Space Administration (NASA;
61 Naftel 2009). Such observations have documented the vertical thermodynamic and kinematic
62 structure of TCs over large mesoscale regions across the entire cyclone and surrounding
63 environment. The mean structure of the HBL has been elucidated through individual and
64 composite dropsonde observations over hurricanes of varying strengths and varying degrees of
65 symmetry (e.g., Franklin et al. 2003; Kepert 2006; Zhang et al. 2011, 2013). In general, it has
66 been found that the top of the dynamic HBL (i.e., the level at which the hurricane radial inflow is
67 10% of its peak value) decreases with height with decreasing radial distance from the center of

68 circulation (Zhang et al. 2011; Giammanco et al. 2012). Wind profiles often exhibit a distinct
69 peak (or jet) within the dynamic HBL, usually near the inner core of the tropical cyclone
70 (Giammanco et al. 2012). Numerical modeling studies have focused on replicating the HBL as
71 observed in nature, often finding that the representation of the HBL is highly sensitive to model
72 diffusion and HBL parameterization schemes (e.g., Xiaodong and Zhemin 2006; Bryan and
73 Rotunno 2009; Nolan et al. 2009a,b).
74 In contrast to the open water HBL, the structure of the HBL across the land-water
75 interface across the coast is not as well documented. Observations over the land surface are
76 limited by aircraft flight safety concerns while the sparse nature of profiling systems over land
77 limit where vertical profiles of the boundary layer may be retrieved. Nonetheless, a few
78 observational studies have been performed (Morrison et al. 2005; Lorsolo et al. 2008;
79 Giammanco et al. 2012; Hirth et al. 2012; Ming et al. 2014). Hirth et al. (2012) found that an
80 internal boundary layer (IBL; c.f., Garratt 1990) formed across the land-ocean interface during
81 the landfall of Hurricane Frances (2004). The IBL resulted from the surface roughness
82 discontinuity across the coastal transition. In general terms, the IBL forms due to a discontinuity
83 in, for example, aerodynamic surface roughness (e.g., an ocean-land interface) as flow passes
84 across the discontinuity (e.g., Garratt 1990; Savelyev and Taylor 2005). All else being equal
85 downwind of the discontinuity, the boundary layer adjusts to the new surface roughness
86 characteristics such that the IBL grows until it represents the complete depth of the fully adjusted
87 boundary layer (see Hirth et al. 2012, their Figure 6). In Hirth et al. (2012), the complexity of the
88 coastal environment and the attendant adjustment of the HBL were examined. Across the coastal
89 interface, the modeled empirical growth of the IBL was observed to be less than expected. Due
90 to inhomogeneities in surface roughness and the added complexity of coastal islands, the

structure of the growing boundary layer was far from homogeneous in their analyses. In addition, significant backing of the low-level (400-500 m) winds was observed in their analyses, with changes in wind direction of 15-20° immediately inland.

Using velocity-azimuth display (VAD) profiles, Giammanco et al. (2012) demonstrated that the evolution of onshore and offshore flow denoted by normalized boundary-layer mean wind profiles were relatively similar. Specifically, the reduction in the boundary layer height with decreasing storm-center-relative radial distance was found for both onshore and offshore regimes. Jet-like features were observed in profiles in both regimes as well, largely tied to regions near the radius of maximum wind (RMW). However, significant differences were found in onshore and offshore wind profile structures for the same normalized radial distances. Surface roughness and upwind terrain characteristics were found to change the vertical structure of the boundary layer significantly. The authors also made mention of jet-like features in outer rainbands, similarly found in Knupp et al. (2006). Neglecting storm-relative space, Krupar et al. (2016) used VAD profiles estimate the surface wind speed in 17 hurricane landfalls. It was found that WSR-88D site-specific constructions of linear regression equations yielded the most accurate surface wind estimates. However, the authors acknowledged that VAD retrievals are limited in assessing HBL characteristics across large spatial regions and emphasized the need for spatially contiguous observations from, for example, dual-Doppler analyses across the coastal region.

Ming et al. (2014) documented fluctuations in HBL structure with the passage of outer rainbands in Typhoon Morakot (2009). Downdrafts associated with rainbands tended to reduce the height of the tangential wind maximum. Contrary to most studies, Ming et al. found that the tangential wind maximum in the outer rainbands was above the height of the dynamic HBL and

114 suggested the observation could be the direct result of landfall processes. However, no study has
115 been able to address the change of the height of the tangential wind maximum while observing
116 both onshore and over water boundary layer structure and the transition between the two. If the
117 observation of the tangential wind maximum above the boundary layer is generally applicable to
118 TC landfalls, then the landfall HBL transition is likely important in the vertical momentum
119 structure observed over land. In particular, the projection of momentum aloft via turbulence on a
120 variety of spatial scales has been shown to be fundamental in the magnitude of gusts observed at
121 the surface (Morrison et al. 2005; Lorsolo et al. 2008; Kosiba and Wurman 2014). Furthermore,
122 individual convective processes such as rainbands are also likely fundamental to the observed
123 vertical distribution of momentum. However, a comparison of the HBL in rainbands to that of
124 the inner core and eyewall has not been examined within an individual storm.
125 In this study, the transition of the HBL, specifically the structure of the sustained wind,
126 during the landfall of Irene (2011) will be documented quantitatively using over-ocean
127 dropsonde observations, land-based VAD retrievals from ground-based Doppler radars, and
128 dual-Doppler wind retrievals. The study is unique in that the observations over land and water
129 were collected within the same time period. Flow regimes in the outer bands, the inner core, and
130 eyewall can also be directly compared. Moreover, one set of VAD winds is from a frequency-
131 agile Doppler radar with a temporal resolution of approximately 30 s and can be used to extend
132 the information extracted from dual-Doppler analyses (available every 10 min). Additionally, the
133 dual-Doppler domain includes portions of the coastal interface. Hence, for the first time, the
134 mean HBL can be examined near simultaneously from over water, through the coastal transition,
135 and inland. Specifically, the transition of the tangential wind maximum will be shown as the
136 HBL changes in response to the coastal surface roughness discontinuity. The coastal transition,

in particular, is herein documented with high temporal and spatial resolution across a limited domain within ± 10 km from the land-water interface and extended through dropsonde and VAD analyses.

2. Data and Methods

Noted in Avila and Cangialosi (2012), Hurricane Irene (2011) began as a tropical wave originating off the coast of Africa on 15 August and became a tropical storm on 21 August east of Dominica. At its most intense period, Irene struck the Bahamas as a Category 3 hurricane (50-58 m s^{-1}) before moving north and beginning to weaken. On 27 August, Irene made landfall near Cape Lookout, NC as a Category 1 storm (estimated 38.6 m s^{-1} maximum sustained 1-min wind at 10 m altitude). In addition to flooding and wind damage experienced in North Carolina, Irene produced tremendous inland flooding in parts of New England before making its extratropical transition at higher latitudes.

During its landfall in North Carolina, simultaneous observations by the NOAA aircraft and ground-based mobile and stationary radars afford the retrieval of boundary layer structure over the open ocean, in coastal waterways, and onshore. At the time of simultaneous observations prior to and during landfall, Irene was considered a Category 1 hurricane with a maximum sustained wind of ~38 m s^{-1}. The observational period (00 to 13 UTC) encompasses the outer bands, inner core (generally the annulus bounded by the RMW wind to a radial approximately three times that of the RMW), and eyewall (c.f., Houze 2010).

a. Dropsondes

159 GPS dropwindsondes (here referred to as "dropsondes") are commonly released by the
160 NOAA P-3 to characterize vertical structure of temperature, relative humidity, pressure, and
161 horizontal and vertical wind speeds and directions in hurricanes (e.g., Franklin et al 2003;
162 Halverson et al. 2006; Stern et al. 2016; Rogers et al. 2017). The details of a dropsonde and its
163 measurement errors can be found in Hock and Franklin (1999) and Zhang et al. (2011, Section
164 2b). Here, the dropsonde kinematic data are especially useful for characterizing the vertical
165 structure of the HBL winds and are exclusively utilized for consistency with other datasets
166 described below. In addition, we interpret the depth of the boundary layer height according to the
167 dynamic definition recommended in Zhang et al. (2011).
168 During Hurricane Irene, the NOAA P-3, the NOAA G-IV (Aberson and Franklin 1999),
169 and Air Force Reconnaissance aircraft conducted a series of flights near landfall that will be the
170 focus of this study (see Figure1a, 1c). Dropsondes used in this study were limited to 27 August
171 2011 to be representative of the environment over water in close proximity to available land-
172 based instrumentation. All dropsondes were processed using the National Center for
173 Atmospheric Research's (NCAR's) Atmospheric Sounding Processing Environment (ASPEN)
174 software as described in Zhang et al. (2013). The fallspeed of a typical dropsonde is 12-14 m s^{-1}
175 and the sampling rate is 2 Hz, yielding 5-7 m vertical sampling. The 2-Hz sample was filtered
176 over 5-s intervals in ASPEN, yielding approximately 10-m resolution.
177
178 *b. SMART Radar and Morehead WSR-88D*
179 The University of Oklahoma (OU) Shared Mobile Atmospheric Research and Teaching
180 (SMART) radar 2 (SR2; Biggerstaff et al. 2005; Biggerstaff et al. 2017) was deployed to
181 Michael J. Smith airfield near Beaufort, NC prior to Hurricane Irene's landfall. SR2 (located at

34.7331°, -76.6619°) operated continuously for approximately 15 hours between 2100 UTC on 26 August and 1215 UTC on 27 August 2011. While SR2 collected data to achieve a variety of science objectives, SR2 radar volumes that were appropriate for performing dual-Doppler analysis with the nearby WSR-88D (Crum and Alberty 1993) in Morehead City, NC (KMHX; located at 34.7760°, -76.8762°) were collected every 10 minutes.

Level II data for KMHX were retrieved from the National Centers for Environmental Information (available at https://www.ncdc.noaa.gov). Dual-Doppler analyses were conducted between 0000 UTC and 1215 UTC on 27 August. While SR2 collected data beginning at 2100 UTC on 26 August, KMHX data between 1800-2359 UTC on 26 August were unavailable, and hence no dual-Doppler analyses were performed. The radial velocities from both radars were objectively dealiased using the region-based dealiasing method available in the Python-ARM Radar Toolkit (Py-ART; Helmus and Collis 2016). SR2 was operated in staggered pulse repetition time (PRT) mode (Torres et al. 2004), which extends the unambiguous Doppler velocity interval. Errors associated with the staggered PRT method were corrected after the radial velocity data were dealiased.

The radar reflectivity (Z_H) and Doppler velocity (V_R) data were interpolated to a Cartesian grid using a Natural Neighbor interpolation (Sibson 1981) method documented in Betten et al. (2018). The Cartesian grid had an origin set to the location of KMHX, with minimum x, y, and z distances of 5, 5, and 0.2 km and maximum x, y, and z distances of 50, 50, and 10.2 km, respectively. The 20-km baseline between the radars provided high spatial resolution over the analysis domain, and horizontal and vertical spacing were set to 250 m and 200 m, respectively. Because the southern dual-Doppler domain was largely affected by ground-clutter from

204 Morehead City, the northern dual-Doppler lobe, which extended over a salt water inlet and open
205 fields, were exclusively used here (Figure1b).
206 The interpolated data were passed into a three-dimensional variational (3DVAR) dual-
207 Doppler analysis technique documented by Potvin et al. (2012). This technique is designed to
208 heavily weigh the observed radial velocity fields when storm-topping echoes are not available
209 (i.e., when the column total mass continuity is under sampled). As the dual-Doppler domain is
210 relegated to below the storm tops at times, this technique is heavily favored for the retrieval of
211 the horizontal winds, rather than traditional, iterative techniques that require better sampling of a
212 column's total divergence profile.
213 In addition to dual-Doppler analysis, range height indicator scans (RHIs) were collected
214 by SR2. However, the azimuths over which the RHIs were taken varied at the discretion of the
215 radar operator. To provide a more consistent set of vertical cross-sections, RHIs were developed
216 from the volumetric scans over a 15° azimuthal sector every 3°, yielding five total RHIs per
217 volume. The radial velocity field was dealiased manually in all cases using Solo3 (Oye et al.
218 1995).
219
220 *c. RaXPol Data*
221 The Rapid X-band dual-Polarimetric radar (RaXPol; Pazmany et al. 2013; Pilke et al.
222 2013) was deployed nearly co-located with SR2 in Beaufort, NC. Using a frequency-agile
223 transmitter, RaXPol collects data at a maximum azimuthal antenna rotation rate of 180° s^{-1}.
224 During the landfall of Irene, RaXPol operated at 120° s^{-1}, yielding one elevation scan every 3 s
225 (excluding time to transition the antenna to the next elevation). RaXPol primarily operated
226 between 00 and 05 UTC, affording high temporal resolution Doppler velocity retrievals of the

HBL within 30 km of the radar's location (34.7300°, -76.6570º) during the landfall of Irene's outer bands. The data were similarly processed through Py-ART's region-based dealiasing scheme. These data were analyzed using a velocity-azimuth display (VAD) technique described below.

d. Coastal VADs

The VAD technique described in Browning and Wexler (1968) was used to construct representative profiles of the boundary layer wind structure from Doppler radar. The technique involves using Doppler velocity observations around constant radii circles to retrieve the mean flow at constant heights. The fit of Fourier coefficients to the radial velocity observations assumes that the flow characteristics around a constant radial circle vary at most linearly across the circle.

The vertical resolution of the constructed vertical profiles is dependent on the radial resolution of the radar data. Profiles were constructed for both KMHX and RaXPol radial velocity observations. KMHX collected data at 250-m radial resolution. Using radial velocity data between 0.15 km and 8.0 km from KMHX, VADs with an average resolution of ~7 m in the vertical were obtained and a maximum resolution of ~85 m. Thus, data were linearly interpolated to 15 m vertical resolution. The temporal resolution was approximately every 5 min for VADs retrieved between 0000 and 1300 UTC on 27 August. RaXPol obtained radial velocity data at much higher temporal and radial resolutions. The vertical resolution varied between 15 and 75 m, so the VAD profiles were linearly interpolated to a resolution of 15 m in the vertical. Radar volumes were obtained approximately every 30 s, yielding high temporal resolution observations

249 of the boundary-layer wind profiles. The observation period of RaXPol was largely confined to
250 0000 to 0500 UTC, during which time the outer bands of Irene were moving on shore.
251
252 **3. Open Water Dropsonde Profiles**
253 To facilitate compositing of the HBL vertical profiles within the storm's dynamic
254 framework, observations of the *RMW* based on stepped frequency microwave radiometer
255 (SFMR; e.g., Uhlhorn and Black 2003) data were used to normalize the radial distance from the
256 center of circulation *(r)* relative to the RMW using (1).

257 $$r^* = \frac{r}{RMW} \qquad (1)$$

258
259 Total wind speed dropsonde observations from 27 August 2011 prior to and during Hurricane
260 Irene's landfall were composited for the lowest 1200 m altitude by the normalized radius r^*.
261 Dropsondes with drop points $0.8 < r^* < 3$ and distances between 0 and 100 km from the nearest
262 point on the coast were retained for this study. This method yielded 10 dropsondes taken within
263 50 km of the nearest coastline (near coast) and 7 dropsondes between 50 and 100 km of the
264 coastline (far coast; Figure 1a). The wind speeds are also normalized by the mean 10-500 m
265 wind speed observed by each dropsonde unless otherwise noted.
266 Although a relatively small sample for each set of coast-relative distances, Figure 2
267 shows the mean normalized profiles for the near and far coast dropsondes. All profiles were
268 taken within 100 km of the coastline and over the North American continental shelf. One
269 dropsonde (highlighted in Figure 1) was dropped just beyond the continental shelf, but is
270 retained as it was very near the gradient in bathymetry. Hence, we take the dropsonde profiles as
271 representative of shoaling wave conditions (Powell et al. 2003), where drag coefficients are

increased relative to deep water (e.g., beyond the continental shelf). Each profile shows normalized wind speed maxima well above the surface. In addition, both regions exhibit mean 10-m normalized winds that are less than 0.8 of the 0-500 m mean flow, similar to past studies (e.g., Kepert 2001). The composite profiles yield several results of note. First, the normalized wind speeds in the lowest 100 m of both near and far coast profiles are significantly more variable than other winds below 500 m, with standard deviations on the order of 0.10-0.15 of the normalized mean wind speed. A similar increase in the variability of the normalized profile was recorded in Giammanco et al. (2012). Secondly, while the magnitudes of the mean 10 m wind speed normalized by the 0-500 m mean are similar for the near coast (0.79; Figure 2a) and far coast (0.76; Figure 2b), the structure of the normalized profiles differ strongly aloft. The near coast profiles exhibit their maximum values around 600-800 m altitude while the far coast wind speeds are maximized at approximately 400 m. The "jet" structure exhibited by both profiles is consistent with previous observations of the HBL observed well over water (e.g., Zhang et al. 2011; Giammanco et al. 2012).

The robustness of the limited observations taken on 27 August was compared using all the dropsondes in Hurricane Irene between 26-28 August 2011 and for $0.8 < r^* < 3.0$ (shown as red lines in Figure 2). However, to generate a larger sample, dropsondes were not delineated according to their coast-relative distance (i.e., dropsondes over the open ocean, well away from the coast were retained). In total, 42 profiles were retained for comparison to the near and far coast profiles (see red lines in Figure 2; referred to as the all-profile-mean). The profile structure below 400 m delineated by coast-relative distance represented the all-profile-mean well. Specifically, the normalized wind speeds at 10 m for the near and far coast profiles were quantitatively similar to the all-profile-mean (differences of ~0.02 to 0.03). In addition, the 10-

295 400 m layer for both near coast and far coast profiles are quantitatively representative of all
296 profiles (differences generally less than 0.05). The height of the maximum normalized wind for
297 all dropsondes was 600-800 m, which matched the near coast profile well. In addition,
298 normalized differences of approximately 0.03-0.05 above a height of 600 m exist for near coast
299 profiles, suggesting the entirety of the near coast profile was generally representative of the
300 dataset. However, some differences aloft were noted in the far coast profiles. The far coast
301 profile appeared to suggest a height of the maximum normalized wind to be near 400 m. It is
302 unclear if the differences between all profiles and the far coast profile were due to sampling
303 differences or the smaller number of dropsondes (7 in total). We hypothesize the differences in
304 sample space (particularly sondes dropped at varying r^*) to be a more plausible reason for
305 differences in the profiles, rather than the sample size itself.
306 The observed dropsonde wind profiles can be decomposed into tangential and radial wind
307 components by projecting the wind direction into a storm-center-relative framework using the
308 method of Willoughby and Chelmow (1982). Uncertainty in the exact center of circulation can
309 affect the estimation of the radial wind more strongly than the tangential wind. Nevertheless, the
310 approach has been used in previous studies (e.g., Giammanco et al. 2012) successfully, as it is
311 based upon center-fixes collected by aircraft operations at higher temporal frequency than
312 National Hurricane Center Best Track estimates. The characteristics of the tangential wind
313 component in the soundings are largely similar to those of the full wind profiles described above
314 (see Figure 3a and b). In contrast, the radial wind profiles (Figure 3c, 3d) exhibit significantly
315 greater variability, likely due to the azimuthal variability in the radial wind. Based on the
316 composite mean, the near coast (0-50 km) profiles (Figure 3c) suggest that the boundary layer
317 height, h_{inflow} ,is approximately 1000 m with the peak tangential (and peak full) wind speed near

800 m altitude (Figure 2a). This is consistent with past observational studies, which have demonstrated that the maximum tangential wind is often located within the inflow layer as shown here (Vickery et al. 2009; Zhang et al. 2011; Montgomery et al. 2014). To examine the transition of the boundary layer from the open ocean to the coast, vertical wind profiles were derived from the dual-Doppler analyses.

4. Coastal Composite Profiles

Since the dual-Doppler domain includes both water and land surfaces, a classification of "land" or "water" was assigned for each dual-Doppler grid point (Figure 4a) using the Basemap function in Python (available online at https://matplotlib.org/basemap). The distance (regardless of wind direction) from the coast was calculated (negative values in Figure 4b indicate inland and positive indicate over coastal waterways). For each dual-Doppler grid point, a vertical profile normalized by the 0-600 m mean wind (slightly different from the dropsondes in Section 3 due to the differing vertical resolution) was constructed. In general, profiles were taken between 10 km inland and 5 km over water (-10 km to +5 km) of the coastline. A subset of the dual-Doppler lobe (shown in Figure 1a) was used in this region. Within the observation period, the mean wind direction across the dual-Doppler domain was between ~70° to ~110° (winds from the east), indicative of onshore flow in the dual-Doppler domain. Since the dual-Doppler subdomain is relatively small, we assume that the water versus land profiles are taken approximately in the same storm-center relative space. However, differences are readily apparent in the mean winds over land and over water as expected with domain-averaged 0-600 m wind speeds less over land than over water (Figures 4c, 4d).

341 *a. Over Water HBL Structure*

342 To examine the coastal transition of the boundary layer throughout the dual-Doppler
343 observation period, the over land and over water profiles were further delineated into subsets
344 representing the distance to the nearest point of coastline. Negative distances indicate profiles
345 over land and positive distances indicate profiles over water. As shown in Figure 4, the water
346 surfaces used here are confined to coastal waterways that experienced easterly flow throughout
347 the dual-Doppler period. At times depending on the exact wind direction, flow may have
348 undergone transition off of land surfaces into the coastal waterways. Nevertheless, flow was
349 generally in an onshore regime across the domain as a whole.

350 The result over the full ~12 h period of the dual-Doppler analysis is shown in Figure 5.
351 The near-shore profiles retrieved by dropsondes in Figure 2 showed a maximum in normalized
352 wind speed above 600 m. Similarly, the dual-Doppler-derived mean profiles just off the coastline
353 indicate the maximum wind speed was between 400 and 800 m in altitude. Indeed, the general
354 structure of the dual-Doppler normalized winds from 0-5 km over water appears similar to the
355 dropsonde-measured boundary layer profiles over water. Specifically, winds between 400-800 m
356 generally exceed the boundary layer mean wind by a few percent. Winds between 200-400 m are
357 generally near 100% of the boundary layer mean wind or just slightly less than the mean wind
358 speed, similar to dropsonde composites. The profiles in the 0-2.5 km range bins change relative
359 to the 2.5-5.0 km range bins, suggesting the HBL may begin to "feel" the shoreline in the 0-2.5
360 km bins. However, it is unclear if this is due to smoothing performed in the interpolation and
361 dual-Doppler analysis, or if the HBL begins adjusting near the shore.

362 To explore the changes seen in the mean profiles over water nearing the coast, RHIs
363 taken by SR2 are employed. Although RHIs can only resolve the one-dimensional wind directly

toward or away from the radar perspective, RHIs of the boundary layer can corroborate the mean structure of the coast-relative boundary layer generated from dual-Doppler analysis. Shown in Figures 6a and 6b, a single RHI taken at 1009 UTC along a rainband exterior of the eyewall (approximately perpendicular to the coast) shows a maximum in V_R (Doppler velocity) between 500-1000 m altitude within 8 km range, where 8 km approximately represents the radar-relative range to the coast (excluding the barrier islands). Beyond 8 km, the V_R maxima appear to be below 500 m altitude. Additionally, V_R appears to be relatively constant below 500 m altitude beyond 8 km. Clearly, the structure of V_R in the plane of the RHI changes abruptly at the coast, rather than transitioning just over water as in the composite dual-Doppler analysis results. Inland from the coast, the maximum V_R increases in height to between 500 and 1000 m above radar level within approximately 2-3 km of the coastline, similar to what is seen in the dual-Doppler analysis mean. Below 500 m, the magnitude of V_R decreases, likely from both the backing of the boundary layer wind and the reduction in the magnitude of the boundary layer wind. Figure 5b corroborates that backing in the plane of the RHI is likely, as the coast-relative mean wind direction in over water bins in the mean is 80-90° compared to onshore values of 70-80° in the lowest 500 m of the atmosphere. This transition occurs rapidly inland of the coastline, suggesting that IBL growth is a function of the discontinuity of surface roughness from water to land surfaces, similar to the results found in Hirth et al. (2012).

An additional RHI (Figure 6c, 6d) was examined 10 minutes (0959 UTC) prior that was further southwest over a similar portion of the coastal region. Doppler velocities were weaker in this case, as the plane of the RHI was not oriented nearly parallel to the boundary layer wind. Nevertheless, at approximately 6 km range (corresponding to the coastal region) in Figures 6c and 6d, the Doppler velocities show a decrease in the V_R field below 500 m and a similar growth

387 in the depth of the weaker V_R structure as in the RHI taken at 1009 UTC. There exists an
388 additional perturbation in V_R at approximately 8.5 km range, which corresponds to the barrier
389 islands shown in the inset in Figure 6d. As at 1009 UTC, the change in the V_R field appears to
390 exist coincident with the coastal interface, suggesting that the HBL winds adjust to the
391 underlying surface while the residual V_R maximum above retains its character.
392
393 *b. Inland HBL Structure*
394 Onshore, rapid changes in the boundary layer mean winds can be seen beginning in the
395 first range bin inland from the coast (Figure 5a). An immediate increase in the altitude of the
396 normalized maximum wind can be seen relative to the over water structure. Winds below 400 m
397 fall below 95% of the boundary layer wind speed. Further inland, winds fall to about 90% of the
398 mean wind at ranges of -10 to -7.5 km. Over land, the height of the maximum tangential wind
399 (Figure 7a) appears to shift from heights of 400-800 m over water to 800-1000 m onshore,
400 suggesting that the surface roughness transition at the coast influences the height of the
401 maximum wind.
402 The actual tangential wind speed profile (Figure 7a) shows a qualitatively similar
403 structure to the normalized total wind (Figure 5a), but the actual radial wind speed profile
404 (Figure 7b) shows the most significant changes relative to the normalized wind. Rather than
405 using a normalized wind value, which is more heavily affected by values between -1 and 0 m s^{-1}
406 (division by a small number), the full radial wind is shown to demonstrate the rapid transition in
407 boundary layer structure across the coast (Figure 7). Between 2.5 and 5 km over water, the
408 maximum radial inflow in the mean is between 200 and 400 m altitude and changes little toward
409 shore, but increases in magnitude over land. As expected, the radial wind onshore should

410 increase for the same total wind speed, as the degree of imbalance between the Coriolis,
411 centrifugal, pressure gradient, and frictional forces is disrupted relative to over the open ocean.
412 The height of the mean boundary layer (defined by the height at which the radial inflow
413 is 10% of its peak value; Zhang et al. 2011) appears to be above the height of the maximum
414 tangential wind for over water profiles. Figure 7b shows that the transition between boundary
415 layer inflow (negative velocities) and outflow (positive velocities) is generally between 600-
416 1000 m altitudes. Between -5 and +2.5 km distance from coast the height of the inflow layer
417 appears to increase relative to the surrounding bins. However, the inflow from 800-1000 m is
418 very weak and is near the 10% criteria, suggesting that by definition the inflow depth is
419 relatively constant across the coastal interface in this analysis. On the other hand, further inland
420 the vertical distance between the maximum tangential wind and the top of the inflow layer
421 appears to diminish from over water to onshore. Between -10 and -5.0 km, the height of the
422 maximum tangential wind resides in the mean outflow layer, which is above the HBL top.
423
424 *c. Coastal Composite Change*
425 Since the evolution of the normalized winds is a function the mean wind, it is useful to
426 characterize the HBL transition in terms of the maximum normalized wind to more
427 comprehensively view the HBL transition at the coastal interface. A time-averaged VAD profile
428 from KMHX taken over the same period as the dual-Doppler analyses is used as a proxy for the
429 HBL downstream of the -10 to -7.5 km range bin in Figure 5a. The individual VADs used in the
430 composite were normalized by the 200-600 m wind to be consistent with the dual-Doppler
431 normalized profiles. Then, for each composite profile (KMHX and each range bin in Figure 5a),
432 the maximum normalized wind was found and the profile was shifted such that the maximum

433 normalized wind was represented by a value of 1.0 (Figure 8a). It is clear that the profiles above
434 800 m altitude adjust little, while the profiles below evolve rapidly as a function of inland
435 distance. This is indicative of IBL growth, as expected across the coast. The top of the "kink" in
436 the profile below the otherwise unaffected winds aloft can be used as a proxy for the height of
437 the growing IBL, which suggests rapid growth of the IBL within 5 km of the coast and relatively
438 slow growth further inland.

439 However, the adjustment of the HBL to the inland surface roughness regime implies that
440 the HBL wind profile through the coastal transition may deviate from a logarithmic profile (or
441 log-linear profile). Over the ocean on average, dropsonde profiles suggest that the HBL is
442 indeed log-linear (e.g., Franklin et al. 2003; Powell et al. 2003; Giammanco et al. 2013). This
443 notion is examined via the dual-Doppler coastal-composite analyses by computing the
444 aerodynamic surface roughness needed to maintain a log-linear profile between 200 m (the
445 lowest available dual-Doppler wind measurement) and the height of the maximum wind
446 (calculated for each profile as a function of distance from the coast). This calculation is done via
447 the time-average full wind speed, not the normalized wind speed. Following the general
448 technique of Kosiba et al. (2013) and Alford et al. (2019) using a wind speed at 200 m V_{200} and
449 the maximum wind speed (V_{max}) a height of z_{max}, the aerodynamic surface roughness z_0 can be
450 calculated by solving for z_0 in (2) to obtain (3).

451 $$V_{200} \ln\left(200/z_0\right) = V_{max} \ln\left(z_{max}/z_0\right) \qquad (2)$$

452 $$z_0 = \exp\left(\left(V_{max} \ln(200) - V_{200} \ln(z_{max})\right) / \left(V_{max} - V_{200}\right)\right) \qquad (3)$$

453 The resulting z_0 are indicated in Figure 8b, which range from <0.001 for over water surfaces and
454 0.001 to 0.37 for over land surfaces, which appear to be reasonable averaged across relatively
455 large spatial areas with complex land use conditions. More importantly, the profiles between 200

m and z_{max} remain mostly log-linear, suggesting that the IBL through the coastal transition remains representative in general of a logarithmic boundary layer.

5. Temporal Evolution of the Coastal HBL

Previous studies often employ the use of mean profiles (as above) to assess the structure of the HBL, either over land or over water. However, the evolution of the HBL in storm-center-relative space has not been examined quantitatively to our knowledge. Here, we examine the temporal evolution of the HBL over land compared to that observed over water using dual-Doppler analyses and available VAD retrievals from RaXPol and KMHX.

a. Dual-Doppler Analysis Results

Using a time series of area-averaged normalized vertical wind profiles, the transition of the mean boundary layer wind speed and depth over land and over water in the dual-Doppler domain can be ascertained. As we discuss the wind speeds in their normalized forms, the area-mean 0-600 m winds are shown in Figure 4c (4d) for land (water) surfaces. However, each dual-Doppler profile at each dual-Doppler analysis grid point is normalized by its own 0-600 m mean wind. Thus, the mean winds shown in Figures 4c and 4d are for general context only. In Figure 9, time periods from approximately 0000 UTC – 0716 UTC on 27 August represent the outer bands of Irene, 0716 UTC – 1046 UTC represents the inner core, and 1046 – 1206 UTC represents the eyewall. These spatial regions were defined by the spatially averaged r^* over the dual-Doppler domain. Normalized radii larger than 3 were considered to be outer bands, 1.5 – 3 was considered inner core, and 0.8 – 1.5 was considered eyewall. Within each of these regions, the structures of the profiles for each regime (outer bands, inner core, and eyewall) differ

strongly from one another. The normalized 0-1200 m wind profiles indicate that the strongest boundary layer winds are generally experienced between 400 and 1200 m heights for all inland profiles, but the height of the maximum wind descends with decreasing radial distance (increasing time) to the eyewall, namely in the inner core and eyewall regimes. Below the inland maximum winds (Figure 9a), the normalized wind at the lowest analysis level between 0000-0700 UTC (outer bands) is generally weaker than in the inner core and eyewall regimes. Additionally, the winds above the maximum in the inner core and eyewall regimes decrease rapidly, which is generally not seen in the outer band regime, indicative of a jet-like profile in the eyewall of Irene. A similar trend is seen in over water profiles, but with stronger mean-wind-relative reductions above the wind maximum during the inner core and eyewall, indicative of a more pronounced wind maximum (i.e., jet-like profile; Figure 9b). This trend has been observed in over water mean profiles in other studies (Franklin et al. 2003; Giammanco et al. 2012). The inner core regime after ~0700 UTC for both land and water profiles shows greater temporal consistency of a jet-like profile in the boundary layer and a gradual decrease in the height of the maximum wind toward the eyewall. As mentioned, the eyewall exhibits a more classic "jet" profile (e.g., Kepert 2001) with maximum normalized winds near 400 m heights over water and 600-800 m inland. Thus, the dual-Doppler analyses reveal unique HBL structures in the outer band, inner core, and eyewall regimes that are qualitatively similar inland and over water, but quantitatively different especially in the lowest analysis levels, where the decay of the wind below the maxima is much greater for inland profiles. In addition, the normalized wind speeds at 200-400 m are notably less than 0.9 for most inland profiles (excluding the eyewall) and generally greater than 0.95 for over water profiles.

501 Wind direction for land and water surfaces in the vertical was also examined (Figures 9e,
502 9f). In all regimes, wind directions over land varied between ~60° and ~90° (from north) at the
503 lowest analysis levels and turned clockwise with height. Similar trends were seen in the over
504 water profiles of wind direction (Figure 9f). While above 600-800 m little difference was found
505 quantitatively in the wind direction for each domain subset, below 600 m altitude a
506 counterclockwise change in the wind direction of 10-20° onshore was observed, similar to the
507 results of Hirth et al. (2012). However, the magnitude of the counterclockwise wind direction
508 change from over water to over land profiles is generally greater in the outer bands and the outer
509 edge of the inner core (differences of 10-15° from 0000-0830 UTC) than in the inner core and
510 eyewall regimes (5-10° from 0835-1200 UTC).
511 Several transient maxima in the 200-400 m normalized wind can be seen both over land
512 and over water in the outer band regime (Figures 9a, 9b), suggesting that the winds relative to the
513 boundary layer mean increase in, perhaps, rainbands. Changes in the wind direction (Figures 9e,
514 9f) and relative peaks in area-averaged wind speeds (Figures 4c, 4d) can also be seen
515 corresponding to changes in the low-level wind structure. Area-averaged radar reflectivity was
516 computed to provide a proxy for periods when the dual-Doppler domain was under the influence
517 of outer rainbands. For low-level (<400 m) normalized wind maxima in the outer band regime
518 (annotated by arrows in Figure 9), reflectivity was generally reduced relative to its surrounding
519 values, suggesting that low-level normalized wind maxima (Figures 9a, 9b), domain-averaged 0-
520 600 m mean wind (Figures 4c, 4d), and wind direction changes (Figures 9e, 9f) were experienced
521 on the edges of rainbands (Figures 9c, 9d). When the area-averaged reflectivity was at a local
522 maximum, the normalized winds often maximized aloft. This result is similar to the results of
523 Ming et al. (2014), who showed that downward turbulent fluxes were often maximized on the

524 exterior of rainbands, leading to the downward transport of high momentum. Retrieved vertical
525 velocity was also explored, but did not show significant trends in an area-averaged sense.
526
527 *b. RaXPol VAD Profiles*
528 To explore the structure of the outer-band regime in greater detail, the structure of the
529 HBL can be examined through VAD retrievals approximately every 30 s to 1 min during the
530 RaXPol operational period. The radial and temporal resolution of RaXPol affords the
531 opportunity to explore the low-level perturbations to the HBL structure (Figure 9) and increases
532 in the area-average winds (Figure 4) that may be associated with rainbands. While turbulence on
533 a variety of scales can also influence the vertical distribution of momentum (Morrison et al.
534 2005; Lorsolo et al. 2008; Kosiba and Wurman 2014; Zhang et al. 2008, 2011), we focus
535 specifically on rainbands here. Based on the time series of dual-Doppler domain averaged HBL
536 structure, it was shown that local maxima in the normalized wind profiles were often associated
537 with gradients in the domain-averaged reflectivity.
538 In Figure 10, a similar time series is shown for 0000 UTC to 0500 UTC documenting the
539 VADs retrieved from radial velocity observations. Figure 10a shows the time series of VAD-
540 derived winds from 0-1200 m at 15 m vertical resolution. Local maxima (minima) in the low
541 levels can be seen and are denoted by solid (dashed) rectangles in Figure 10a. During these
542 periods, winds in the lowest 100 m of the profiles tend to be between 15-20 m s^{-1} relative to
543 surrounding local minima of 10-15 m s^{-1}. These local minima appear to be sometimes in the
544 presence of local maxima aloft, suggesting that high momentum air is seen during these periods
545 at lower levels relative to surrounding times through the observed column.

546 The reflectivity structure observed by RaXPol was examined in context of these wind
547 maxima (minima) to deduce if rainband and convective structures were responsible for these
548 perturbations to the wind field. For the example times denoted in Figure 10a, the wind maxima
549 (minima) are highlighted in Figure 10b over the vertical reflectivity structure. During the periods
550 of local wind maxima denoted in the figure, rainband passage is observed in the vertical structure
551 of the reflectivity. To a degree in the low levels (denoted by black rectangles in Figure 10a) and
552 in the upper levels (denoted by black ovals in Figure 10a) of the VAD profiles, the wind maxima
553 appear to be offset from the reflectivity maxima, suggesting that many of the local wind maxima
554 are experienced on the edges of deep convection. One maximum between 0033 and 0045 UTC
555 appears to be in a core of reflectivity, which resembles precipitation-induced downdrafts
556 previously seen in airborne kinematic retrievals of convection in the outer bands (Barnes et al.
557 1983, 1991). This suggests larger-scale kinematics rainbands and/or convective scale kinematics
558 are responsible for the low-level perturbations to the wind field. Particularly for the local
559 maxima observed aloft, these appear to resemble the wind field perturbations observed by the
560 spatially averaged time series of dual-Doppler analyses in the outer bands (Figure 9). Since the
561 perturbations exist primarily on gradients in reflectivity where downdrafts are anticipated, we
562 expect that the downward flux of high momentum as in Ming et al. (2014) is likely an important
563 mechanism for the local enhancements to the near-surface winds. It has also been observed that
564 gust factors are higher in rainbands (e.g., Schroeder et al. 2009; Giammanco et al. 2016), to
565 which this analysis lends support. As the dual-Doppler composite results and VADs represent
566 horizontal scales of flow larger than, for example, HBL rolls (e.g., Kosiba and Wurman 2014),
567 we interpret the results here as predominantly associated with larger-scale (i.e., rainband)

568 processes. Nevertheless, we anticipate that smaller-wavelength features in the HBL also
569 contribute perturbations to the HBL wind structure, which will be discussed in Section 6.
570
571 *c. KMHX VAD Profiles*
572 The coastal WSR-88D was downstream from the profiles discussed in Section 4b,
573 suggesting that its time varying mean profiles can be used to characterize wind profiles further
574 inland relative to those within 10 km of the coastline (approximately 18 km from the nearest
575 saltwater inlet to KMHX's north). A time series of VADs from KMHX (Figure 11) was
576 constructed to compare the normalized boundary layer winds to the dual-Doppler area-averaged
577 time series shown in Figure 9a. Indeed, the KMHX VADs replicate the regimes observed in the
578 dual-Doppler results well. Between 0000 UTC and around 0730 UTC, the normalized winds are
579 maximized near 1000 m. Between ~0730 UTC to ~1030 UTC, the inner core regime shows
580 maximum winds between 600–850 m, similar to the dual-Doppler analysis results. Finally, the
581 eyewall regime after ~1030 UTC shows the maximum normalized wind near 700 m initially and
582 decreases in height to 300-500 m nearer 1200 UTC. Relatively stronger normalized flow also
583 characterizes the low levels of the retrievals compared to earlier times. However, the magnitude
584 of the ~200 m normalized wind is greater in the VADs than in the dual-Doppler analysis results
585 due to the contribution of the winds below 200 m to the 0-500 m boundary layer mean wind. The
586 VAD winds near 200 m are characterized by values near 100% of the mean wind rather than 0.9
587 or less in the dual-Doppler analyses (Figure 9a). The lowest analysis level (representative of 50-
588 65 m altitude) suggests that the winds in the outer bands fluctuate between 50-60% of the mean
589 wind (with similar time varying perturbations seen to those characterized by the RaXPol VADs

and dual-Doppler time series). In the inner core and eyewall, however, the magnitude of the 70-120 m normalized wind increases to 65-75% of the boundary layer mean at times.

Delineated by distance to the center of circulation, Figures 12 and 13 show the VAD-derived boundary layer winds averaged over time for radial and tangential profiles, respectively. Unlike the dropsonde profiles (Figures 3c and 3d), the radial winds derived from KMHX exhibit a layer of maximum radial inflow above the surface (generally between 200 and 400 m). The normalized tangential profiles (not shown) indicate that the 200-400 m winds are generally 90-100% of the boundary layer mean wind, similar to the dual-Doppler and VAD results discussed previously. The dual-Doppler coast-relative composites suggest that the maximum tangential wind speed first resides in or near the top of the inland HBL within 5 km of the coast, but transitions to above the HBL 5-10 km inland. Given that KMHX is downstream of the dual-Doppler observations and further inland, the maximum tangential wind speed should also be expected to reside near or above the HBL. Indeed, within 100 km of the storm's center of circulation (Figures 12a, b and 13a, b), the height of the inflow layer and the maximum tangential wind speed is approximately at the same altitude (600 m). For profiles taken farther away from the storm center, (Figures 12c, d and 13c, d), maximum tangential wind height (800-1000 m) is well above the top of the HBL. This suggests that the vertical displacement between the maximum tangential wind and the top of the HBL increases with distance from the center of circulation over land.

6. Discussion and Conclusions

As found in Ming et al. (2014) and Marks et al. (2020), the height of the boundary layer over land is increased relative to over-ocean boundary layer structure and resides above the

613 inflow layer. Prior studies such as Ming et al. (2014) suggest that the tangential wind maximum
614 above the inflow layer is a direct consequence of the adjustment of the HBL to changing surface
615 characteristics (i.e., IBL growth). However, the process by which the HBL transitions across the
616 coastal region was not documented. Hirth et al. (2012) showed that the coastal region represents
617 a discontinuity in surface roughness. Their work focused on HBL change observed inland, but
618 offered limited comparison of the HBL structure over water.

619 Here, using high spatial-resolution observations of the HBL relative to the coastline, the
620 transition of the boundary layer characteristics at the coastal interface were examined, which
621 resulted in several key conclusions:

622 1. Using a unique dropsonde, dual-Doppler, and VAD dataset, quantitative differences in
623 the HBL winds were documented. It was shown that the evolution of the HBL was
624 qualitatively similar over water and over land, but their magnitudes were significantly
625 different for all regimes (outer bands, inner core, and eyewall).
626 2. Past studies focused on VAD or boundary layer profiler (i.e., point profiles) retrievals
627 have shown that downdrafts on the periphery of outer rainbands can lead to a reduction in
628 the height of the maximum wind. Based on the mean structure throughout the dual-
629 Doppler domain corroborated by coincident VAD retrievals, this dataset suggests that
630 rainbands are indeed responsible for an enhancement in the lower HBL winds.
631 3. VAD-based studies have suggested that the maximum wind over land resides atop the
632 HBL, rather than within it as over the open ocean. The data herein document that the
633 growth of the IBL is directly responsible for mixing out the previous tangential maximum
634 over the open ocean, wherein the tangential winds above the newly adjusted IBL/HBL
635 become the maximum.

4. As the IBL grows, the wind profile below the maximum likely remains mostly logarithmic as the HBL responds to the inland, large-scale surface roughness change.

Figure 14 summarizes the key observations that resulted from this analysis. Between 0 and 5 km over water the maximum tangential wind was observed to reside in the inflow layer (HBL; see Figure 7) similar to past observations near the coast and over shallow and deep water (e.g., Zhang et al. 2011; Hirth et al. 2012). In the first 5 km inland of the coast, the height of the maximum tangential wind (Figure 7a) is still within the inflow (boundary layer; Fig 9b) as the HBL responds to the discontinuity in surface roughness at the coast (i.e., IBL growth; Figure 14). However, these results suggest that the residual boundary layer does not immediately adjust to the underlying surface, similar to the results of Hirth et al. (2012). Thus, for a period the tangential wind maximum may continue to reside in the inflow layer until the HBL over land has fully adjusted to its underlying surface (Figure 14). RHIs from SR2 support that the adjustment of the HBL begins rapidly in the first few kilometers inland of the coast, similar to the mean coast-relative profiles. The V_R maximum observed in the lowest 500 m of the RHIs over water appeared to increase in height onshore where the IBL growth was occurring. Alford et al. (2019) and Fernandez-Caban et al. (2019), for example, showed that in convective perturbations in the eyewall can represent the strongest winds during the landfall process. Downdrafts in the region may more readily project stronger momentum aloft in the near-coastal regions toward the surface prior to the full adjustment of the HBL to the increased surface roughness inland of the coast. While most observational studies suggest that gust factors immediately inland of the coast do not significantly depart from the mean, Giammanco et al. (2016) support the notion that the wind maximum within the HBL is, perhaps, an upper bound on the magnitude surface winds.

659 Additional data are needed, however, to fully explore this idea. However, changes in the
660 boundary layer structure in time (Figures 9 and 10) are indeed noted in the outer bands, where
661 rainband passage procures the strongest winds in the low levels relative to their boundary-layer
662 means in a domain-wide sense. This study focused on larger scale structures that can be
663 examined through the mean HBL structure, rather than kilometer and sub-kilometer features that
664 also impact the vertical distribution of horizontal momentum (Morrison et al. 2005; Lorsolo et al.
665 2008; Zhang et al. 2008; Kosiba and Wurman 2014). This topic will be addressed in future work.
666 This work augments the mean profile studies referenced herein, which show a strong
667 reduction in the near-surface boundary layer wind relative to its peak aloft. Here, it is found that
668 periods of convection result in greater linearity of the boundary layer profile over water above
669 200 m as shown by dual-Doppler analysis (e.g., Figure 9). While dual-Doppler observations
670 cannot be used to directly retrieve the standardized 10 m wind, the result suggests that pre-
671 convective periods may procure the strongest near-surface winds in the outer bands, supported
672 by the lower-level retrievals procured by RaXPol and KMHX VADs. Based on past studies,
673 greater downward momentum flux on the edges of convection in the outer bands is likely
674 responsible for the transition of a sharply decreasing profile relative to the boundary layer
675 maximum wind to a gradual reduction in the boundary layer wind relative to its above maximum.
676 In contrast, perturbations to the low-level winds were not seen in the inner core regime, but the
677 height of the maximum wind was indeed reduced between the outer bands and the inner core.
678 The eyewall regime transitioned to a strong jet-like profile with a maximum below 500 m in this
679 case. The highest normalized winds in the lowest 100 m of the atmosphere were found in the
680 eyewall regime retrieved by VADs from KMHX. Although addressed to some degree, it is still
681 unclear how the winds near the surface (10 m altitude) evolve relative to the mean winds aloft

682 due to a lack of high resolution (e.g., 200-250 m resolution) dual-Doppler analyses (Krupar et al.
683 2016). While Krupar et al. (2016) found that a logarithmic profile did not represent the HBL as
684 well as a linear-regression fit, this work suggests a log-profile was generally applicable in
685 Hurricane Irene at dual-Doppler analysis levels. Thus, future work should focus on
686 characterizing the complete boundary layer structure from the surface through the top of the
687 HBL onshore and near the shore. As the Texas Tech University StickNets and FCMP 10-m
688 towers were available during the landfall of Irene, our dataset is ideal for comparison in a future
689 study.

690 This work represents a high spatiotemporal resolution observational case study in a
691 gradually weakening TC, but emphasizes for the need additional observations of the boundary
692 layer during TC landfalls. The general conclusions from this work should be studied in stronger
693 storms to assess the generality of the results across various TC intensities. Over the open ocean,
694 boundary layer structure is not only a function of radial distance from the eyewall or shear-
695 relative quadrants, but also a function of TC intensity. Thus, we anticipate similar results may
696 also apply at landfall.

697

698 Acknowledgements: This work was partially supported by RAPID grants AGS-1759479 and
699 AGS-1902593 from the National Science Foundation and by the National Institute of Standards
700 and Technology under grant number 70NANB19H056. We also thank three anonymous
701 reviewers for their constructive comments that improved the quality of this manuscript. The first
702 author was supported by NASA Headquarters under the NASA Earth and Space Science
703 Fellowship Program – Grants 17-EARTH17R-72 and 18-EARTH18R-0086. Jun Zhang was
704 supported by NSF Grant AGS1822128 and NOAA Grant NA14NWS4680030. NOAA authors

were also supported by AOML/HRD. SMART radar data and RaXPol VADs are available at the Zenodo Archive doi:10.5281/zenodo.3494891. HRD archived dropsondes are available at https://www.aoml.noaa.gov/hrd/data_sub/. RaXPol is maintained and operated by the Advanced Radar Research Center (ARRC) of the University of Oklahoma.

References

Aberson, S. D., and J. L. Franklin, 1999: Impact on Hurricane Track and Intensity Forecasts of GPS Dropwindsonde Observations from the First-Season Flights of the NOAA Gulfstream-IV Jet Aircraft. *Bull. Am. Meteorol. Soc.*, **80**, 421–427, doi:10.1175/1520-0477(1999)080<0421:IOHTAI>2.0.CO;2.

——, M. L. Black, R. A. Black, R. W. Burpee, J. J. Cione, C. W. Landsea, and F. D. Marks, 2006: Thirty years of tropical cyclone research with the NOAA P-3 aircraft. *Bull. Am. Meteorol. Soc.*, **87**, 1039–1055, doi:10.1175/BAMS-87-8-1039.

Alford, A. A., M. I. Biggerstaff, G. D. Carrie, J. L. Schroeder, B. D. Hirth, and S. M. Waugh, 2019: Near-surface maximum winds during the landfall of Hurricane Harvey. *Geophys. Res. Lett.*, **46**, doi:10.1029/2018GL080013.

Avila, L. A., and J. Cangialosi, 2012: *Tropical Cyclone Report: Hurricane Irene (AL092011)*. 45 pp. http://www.nhc.noaa.gov/data/tcr/AL092011_Irene.pdf.

Barnes, G. M., E. J. Zipser, D. Jorgensen, and F. Marks, 1983: Mesoscale and convective structure of a hurricane rainband. *J. Atmos. Sci.*, **40**, 2125–2137, doi:10.1175/1520-0469(1983)040<2125:MACSOA>2.0.CO;2.

——, J. F. Gamache, M. A. Lemone, and G. J. Stossmeister, 1991: A convective cell in a

728 hurricane rainband. *Mon. Weather Rev.*, **119**, 776–794, doi:10.1175/1520-
729 0493(1991)119<0776:ACCIAH>2.0.CO;2.
730 Betten, D. P., M. I. Biggerstaff, and C. L. Ziegler, 2018: Three-Dimensional Storm Structure and
731 Low-Level Boundaries at Different Stages of Cyclic Mesocyclone Evolution in a High-
732 Precipitation Tornadic Supercell. **2018**, 24 pp, doi:10.1155/2018/9432670.
733 Biggerstaff, M. I., and Coauthors, 2005: The Shared Mobile Atmospheric Research and
734 Teaching Radar: A Collaboration to Enhance Research and Teaching. *Bull. Am. Meteorol.*
735 *Soc.*, **86**, 1263–1274, doi:10.1175/BAMS-86-9-1263.
736 Browning, K. A., and R. Wexler, 1968: The determination of kinematic properties of a wind
737 field using Doppler radar. *J. Appl. Meteorol.*, **7**, 105–113, doi:10.1175/1520-
738 0450(1968)007%3C0105:TDOKPO%3E2.0.CO;2.
739 Bryan, G. H., and R. Rotunno, 2009: The maximum intensity of tropical cyclones in
740 axisymmetric numerical model simulations. *Mon. Weather Rev.*, **137**, 1770–1789,
741 doi:10.1175/2008MWR2709.1.
742 Crum, T. D., and R. L. Alberty, 1993: The WSR-88D and the WSR-88D Operational Support
743 Facility. *Bull. Am. Meteorol. Soc.*, **74**, 1669–1687, doi:10.1175/1520-
744 0477(1993)074<1669:TWATWO>2.0.CO;2.
745 Elliott, W. P., 1958: The growth of the atmospheric internal boundary layer. *Eos, Trans. Am.*
746 *Geophys. Union*, **39**, 1048–1054, doi:10.1029/TR039i006p01048.
747 Fernandez-Caban, P. L., and Coauthors, 2019: Observing Hurricane Harvey's eyewall at
748 landfall. *Bull. Am. Meteorol. Soc.*, doi:10.1175/BAMS-D-17-0237.1.
749 Franklin, J. L., M. L. Black, and K. Valde, 2003: GPS Dropwindsonde Wind Profiles in
750 Hurricanes and Their Operational Implications. *Weather Forecast.*, **18**, 32–44,

751 doi:10.1175/1520-0434(2003)018<0032:GDWPIH>2.0.CO;2.
752 Garratt, J. R., 1990: The internal boundary layer - A review. *Boundary-Layer Meteorol.*, **50**,
753 171–203, doi:10.1007/BF00120524.
754 Giammanco, I. M., J. L. Schroeder, and M. D. Powell, 2012: GPS Dropwindsonde and WSR-
755 88D Observations of Tropical Cyclone Vertical Wind Profiles and Their Characteristics.
756 *Weather Forecast.*, **28**, 77–99, doi:10.1175/waf-d-11-00155.1.
757 ——, ——, F. J. Masters, P. J. Vickery, R. J. Krupar, and J. A. Balderrama, 2016: Influences on
758 observed near-surface gust factors in landfalling U.S. Gulf coast hurricanes: 2004-08. *J.*
759 *Appl. Meteorol. Climatol.*, **55**, 2587–2611, doi:10.1175/JAMC-D-16-0053.1.
760 Halverson, J. B., J. Simpson, G. Heymsfield, H. Pierce, T. Hock, and L. Ritchie, 2006: Warm
761 Core Structure of Hurricane Erin Diagnosed from High Altitude Dropsondes during
762 CAMEX-4. *J. Atmos. Sci.*, **63**, 309–324, doi:10.1175/JAS3596.1.
763 http://journals.ametsoc.org/doi/abs/10.1175/JAS3596.1.
764 Helmus, J. J., and S. M. Collis, 2016: The Python ARM Radar Toolkit (Py-ART), a Library for
765 Working with Weather Radar Data in the Python Programming Language. *J. Open Res.*
766 *Softw.*, **4**, e25, doi:10.5334/jors.119.
767 Hirth, B. D., J. L. Schroeder, C. C. Weiss, D. a. Smith, and M. I. Biggerstaff, 2012: Research
768 Radar Analyses of the Internal Boundary Layer over Cape Canaveral, Florida, during the
769 Landfall of Hurricane Frances (2004). *Weather Forecast.*, **27**, 1349–1372,
770 doi:10.1175/WAF-D-12-00014.1. http://journals.ametsoc.org/doi/abs/10.1175/WAF-D-12-
771 00014.1.
772 Hock, T. F., and J. L. Franklin, 1999: The NCAR GPS dropwindesonde. *Bull. Am. Meteorol.*
773 *Soc.*, **80**, 407–420, doi:10.1175/1520-0477(1999)080<0407:TNGD>2.0.CO;2.

774 Houze, R. A., 2010: Clouds in Tropical Cyclones. *Mon. Weather Rev.*, **138**, 293–344,
775 doi:10.1175/2009MWR2989.1.
776 http://journals.ametsoc.org/doi/abs/10.1175/2009MWR2989.1.
777 Kepert, J., 2001: The Dynamics of Boundary Layer Jets within the Tropical Cyclone Core . Part
778 I : Linear Theory. *J. Atmos. Sci.*, **58**, 2469–2484, doi:10.1175/1520-
779 0469(2001)058<2469:TDOBLJ>2.0.CO;2.
780 Kosiba, K., J. Wurman, F. J. Masters, and P. Robinson, 2013: Mapping of Near-Surface Winds
781 in Hurricane Rita Using Finescale Radar, Anemometer, and Land-Use Data. *Mon. Weather*
782 *Rev.*, **141**, 4337–4349, doi:10.1175/MWR-D-12-00350.1.
783 http://journals.ametsoc.org/doi/abs/10.1175/MWR-D-12-00350.1.
784 Kosiba, K. A., and J. Wurman, 2014: Finescale dual-Doppler analysis of hurricane boundary
785 layer structures in hurricane Frances (2004) at landfall. *Mon. Weather Rev.*, **142**, 1874–
786 1891, doi:10.1175/MWR-D-13-00178.1.
787 Krupar, R. J., J. L. Schroeder, D. A. Smith, S.-L. Kang, and S. Lorsolo, 2016: A Comparison of
788 ASOS Near-Surface Winds and WSR-88D-Derived Wind Speed Profiles Measured in
789 Landfalling Tropical Cyclones. *Weather Forecast.*, **31**, 1343–1361, doi:10.1175/WAF-D-
790 15-0162.1. http://journals.ametsoc.org/doi/10.1175/WAF-D-15-0162.1.
791 Lorsolo, S., J. L. Schroeder, P. Dodge, and F. Marks, 2008: An Observational Study of
792 Hurricane Boundary Layer Small-Scale Coherent Structures. *Mon. Weather Rev.*, **136**,
793 2871–2893, doi:10.1175/2008MWR2273.1.
794 http://journals.ametsoc.org/doi/abs/10.1175/2008MWR2273.1.
795 Marks, F. D., J. A. Zhang, and P. Dodge, 2020: The atmospheric boundary layer wind structure
796 at the landfall of Hurricane Fran (1996) from WSR-88D radar observations. *Mon. Wea.*

Rev., near submission.

Ming, J., J. A. Zhang, R. F. Rogers, F. D. Marks, Y. Wang, and N. Cai, 2014: Multiplatform observations of boundary layer structure in the outer rainbands of landfalling typhoons. *J. Geophys. Res. Atmos.*, **119**, 7799–7814, doi:doi:10.1002/2014JD021637.

Montgomery, M. T., J. A. Zhang, and R. K. Smith, 2014: An analysis of the observed low-level structure of rapidly intensifying and mature hurricane Earl (2010). *Q. J. R. Meteorol. Soc.*, **140**, 2132–2146, doi:10.1002/qj.2283.

Morrison, I., S. Businger, F. Marks, P. Dodge, and J. A. Businger, 2005: An observational case for the prevalence of roll vortices in the hurricane boundary layer. *J. Atmos. Sci.*, **62**, 2662–2673, doi:10.1175/JAS3508.1.

Naftel, J. C., 2009: *NASA Global Hawk: A New Tool for Earth Science Research*. 13 pp. http://ntrs.nasa.gov/archive/nasa/casi.ntrs.nasa.gov/20090023138.pdf.

Nolan, D. S., D. P. Stern, and J. A. Zhang, 2009a: Evaluation of planetary boundary layer parameterizations in tropical cyclones by comparison of in situ observations and high-resolution simulations of Hurricane Isabel (2003). Part II: Inner-core boundary layer and eyewall structure. *Mon. Weather Rev.*, **137**, 3675–3698, doi:10.1175/2009MWR2786.1.

——, J. A. Zhang, and D. P. Stern, 2009b: Evaluation of planetary boundary layer parameterizations in tropical cyclones by comparison of in situ observations and high-resolution simulations of Hurricane Isabel (2003). Part I: Initialization, maximum winds, and the outer-core boundary layer. *Mon. Weather Rev.*, **137**, 3651–3674, doi:10.1175/2009MWR2785.1.

Oye, R. C., C. Mueller, and S. Smith, 1995: Software for radar translation, visualization, editing, and interpolation. *27th Conference on Radar Meteorology*, Vail, CO, Amer. Meteor. Soc.,

359–361.

Pazmany, A. L., J. B. Mead, H. B. Bluestein, J. C. Snyder, and J. B. Houser, 2013: A mobile rapid-scanning X-band polarimetric (RaXPol) doppler radar system. *J. Atmos. Ocean. Technol.*, **30**, 1398–1413, doi:10.1175/JTECH-D-12-00166.1.

Potvin, C. K., D. Betten, L. J. Wicker, K. L. Elmore, and M. I. Biggerstaff, 2012: 3DVAR vs. traditional dual-Doppler wind retrievals of a simulated supercell thunderstorm. *Mon. Weather Rev.*, 120525114116000, doi:10.1175/MWR-D-12-00063.1.

Powell, M. D., P. J. Vickery, and T. A. Reinhold, 2003: Reduced drag coefficient for high wind speeds in tropical cyclones. *Nature*, **422**, 279–283, doi:10.1038/nature01481.

Rogers, R. F., and Coauthors, 2017: Rewriting the tropical record books: The extraordinary intensification of Hurricane Patricia (2015). *Bull. Am. Meteorol. Soc.*, **98**, 2091–2112, doi:10.1175/BAMS-D-16-0039.1.

Savelyev, S. A., and P. A. Taylor, 2005: Internal boundary layers: I. Height formulae for neutral and diabatic flows. *Boundary-Layer Meteorol.*, **115**, 1–25, doi:10.1007/s10546-004-2122-z.

Schroeder, J., B. Edwards, and I. Giammanco, 2009: Observed tropical cyclone wind flow characteristics. *Wind Struct.*, **12**, doi:10.12989/was.2009.12.4.349.

Sibson, R., 1981: A brief description of natual neighbor interpolation. *Interpreting Multivariate Data*, John Wiley, 21–36.

Stern, D. P., G. H. Bryan, and S. D. Aberson, 2016: Extreme Low-Level Updrafts and Wind Speeds Measured by Dropsondes in Tropical Cyclones. *Mon. Weather Rev.*, **144**, 2177–2204, doi:10.1175/MWR-D-15-0313.1. http://journals.ametsoc.org/doi/10.1175/MWR-D-15-0313.1.

Tang, X., and Z. Tan, 2006: Boundary-layer wind structure in a landfalling tropical cyclone. *Adv.*

Atmos. Sci., **23**, 737–749, doi:10.1007/s00376-006-0737-3.

Torres, S. M., Y. F. Dubel, and D. S. Zrnić, 2004: Design, implementation, and demonstration of a staggered PRT algorithm for the WSR-88D. *J. Atmos. Ocean. Technol.*, **21**, 1389–1399, doi:10.1175/1520-0426(2004)021<1389:DIADOA>2.0.CO;2.

UCAR/NCAR, 2005: *NSF/NCAR GV HIAPER Aircraft*. http://doi.org/10.5065/D6DR2SJP.

Uhlhorn, E. W., and P. G. Black, 2003: Verification of remotely sensed sea surface winds in hurricanes. *J. Atmos. Ocean. Technol.*, **20**, 99–116, doi:10.1175/1520-0426(2003)020<0099:VORSSS>2.0.CO;2.

Vickery, P. J., D. Wadhera, M. D. Powell, and Y. Chen, 2009: A hurricane boundary layer and wind field model for use in engineering applications. *J. Appl. Meteorol. Climatol.*, **48**, 381–405, doi:10.1175/2008JAMC1841.1.

Williams, G. J., 2019: Idealized Simulations of the Inner Core Boundary Layer Structure in a Landfalling Tropical Cyclone. Part I: Kinematic Structure. *Trop. Cyclone Res. Rev.*, **8**, 47–67, doi:10.1016/j.tcrr.2019.07.006. http://dx.doi.org/10.1016/j.tcrr.2019.07.006.

Willoughby, H. E., and M. B. Chelmow, 1982: Objective Determination of Hurricane Tracks from Aircraft Observations. *Mon. Weather Rev.*, **110**, 1298–1305, doi:10.1175/1520-0493(1982)110<1298:odohtf>2.0.co;2.

Wurman, J., and J. Winslow, 1998: Intense sub-kilometer-scale boundary layer rolls observed in hurricane Fran. *Science (80-.).*, **280**, 555–557, doi:10.1126/science.280.5363.555.

Zhang, J. A., R. F. Rogers, D. S. Nolan, and F. D. Marks, 2011: On the Characteristic Height Scales of the Hurricane Boundary Layer. *Mon. Weather Rev.*, **139**, 2523–2535, doi:10.1175/MWR-D-10-05017.1.

——, ——, P. D. Reasor, E. W. Uhlhorn, and F. D. Marks, 2013: Asymmetric Hurricane

866 Boundary Layer Structure from Dropsonde Composites in Relation to the Environmental
867 Vertical Wind Shear. *Mon. Weather Rev.*, **141**, 3968–3984, doi:10.1175/mwr-d-12-00335.1.
868 ——, K. B. Katsaros, P. G. Black, S. Lehner, J. R. French, and W. M. Drennan, 2008: Effects of
869 roll vortices on turbulent fluxes in the hurricane boundary layer. *Bound.-Layer*
870 *Meteor.*, **128**, 173–189.
871
872

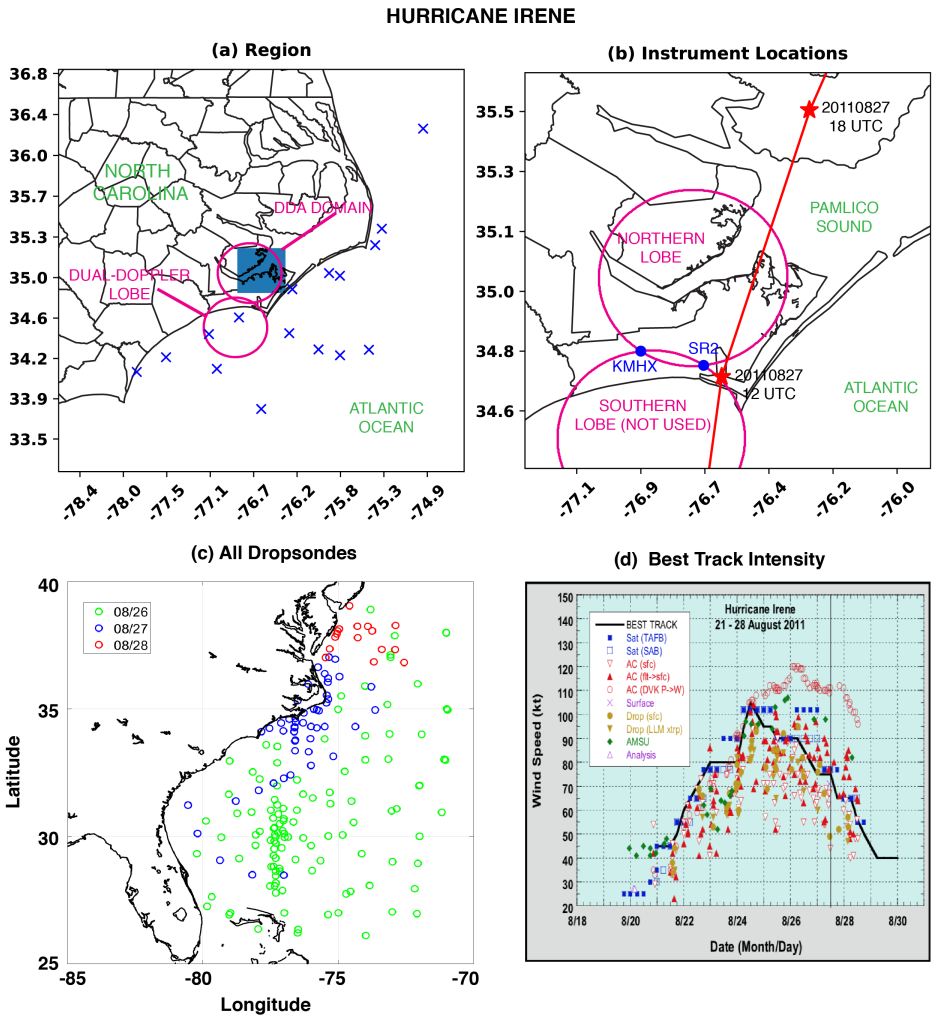

Figure1. Details of the observation, instrumentation, and dual-Doppler domain locations. (a) A large view of the region over which observations were collected. The blue x's indicate locations of dropsondes released by the NOAA P-3 within 100 km of the coast that were used in this study. (b) A detailed view of the dual-Doppler lobes (magenta lines) and the locations of KMHX and SR2 (blue circles). RaXPol was co-located with SR2. The red line indicates the Best Track locations of Irene with synoptic dates and times indicated by the red stars. (c) The locations of dropsondes released by the NOAA P-3, G-IV, and Air Force C-130 are shown colored by date. (d) The National Hurricane Center Best Track intensity in time (figure courtesy of Avila and Cangialosi 2012).

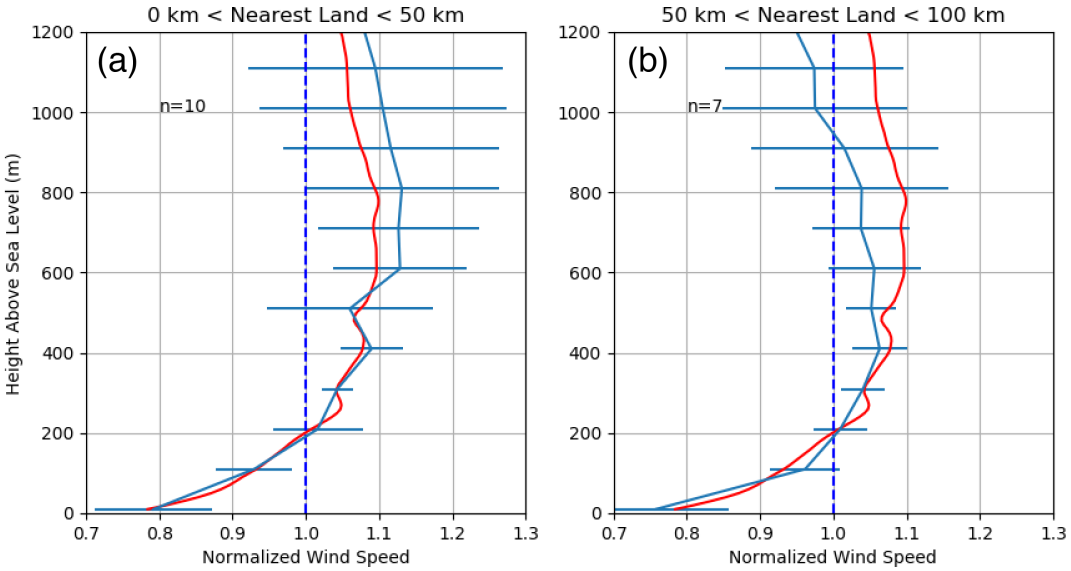

Figure 2. Normalized dropsonde profiles taken (a) from 0-50 km of the nearest point on the coast and (b) 50-100 km of the nearest point on the coast. The dashed blue line indicates a normalized wind speed of 1.0. The cyan line shows the mean of *n* profiles taken for each distance subset on 27 August 2011. The red line indicates the mean of all dropsondes profiles regardless of date. Error bars are ±1 standard deviation.

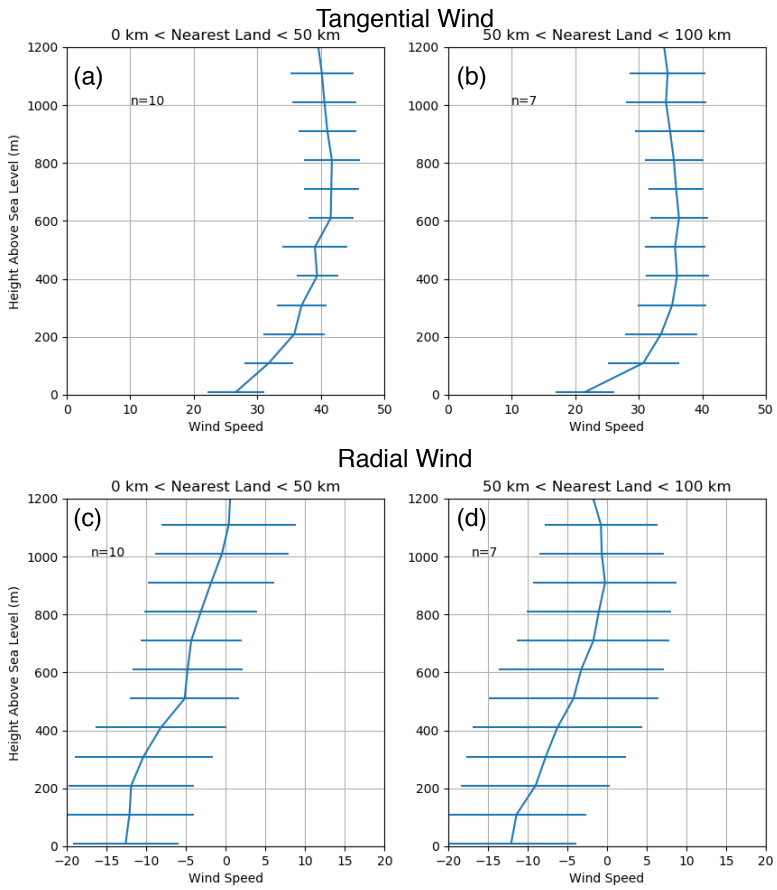

892

893 Figure 3. Dropsondes profiles of non-normalized (a-b) tangential and (c-d) radial wind (relative

894 to the SFMR/Best Track-derived center of circulation) on 27 August 2011. Unlike Figure 2,

895 the actual wind speed values are shown instead of the normalized wind (values in m s^{-1}).

896

897

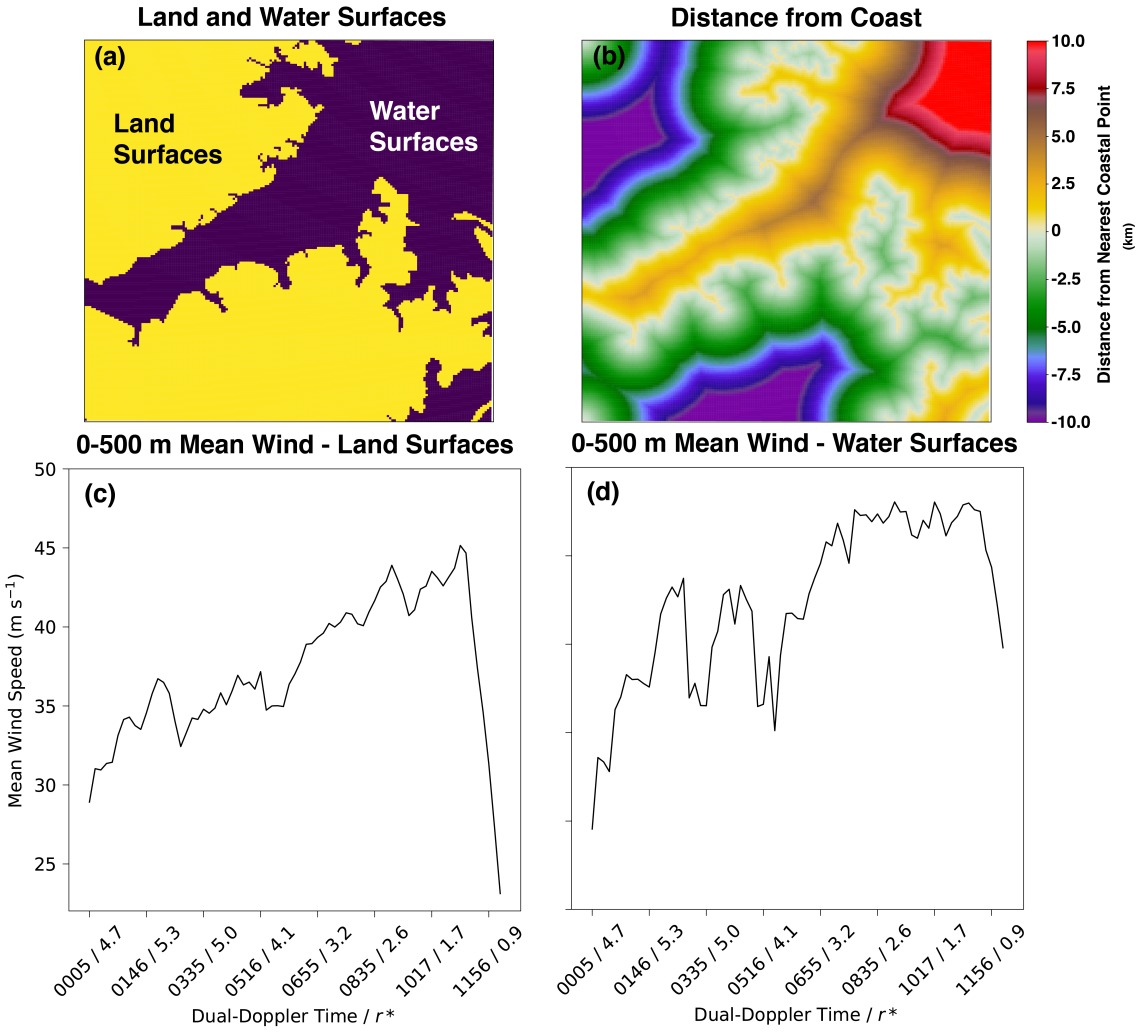

Figure 4. Details of the dual-Doppler domain land and water surfaces. (a) Land surfaces are shown in yellow and water surfaces are shown in purple. (b) For each grid point in the dual-Doppler domain, the distance to the nearest coastal point is shown according to the color bar values (in km). Positive values indicate distances of water surfaces from the coast. (c) A time series of the area-average 0-600 m wind speed across the dual-Doppler domain is shown strictly for land surfaces. (d) As in (c), but for water surfaces. In (c) and (d) the x-axis shows the dual-Doppler time and the domain-mean r*.

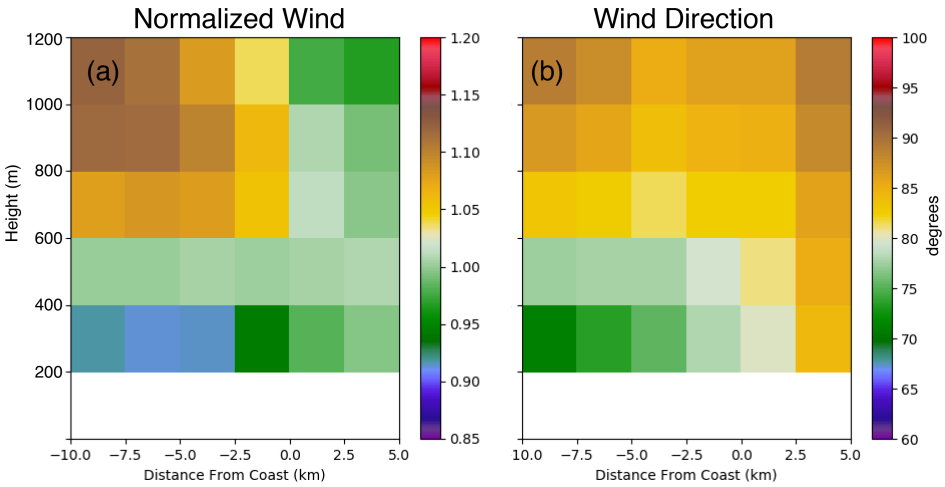

906

907 Figure 5. (a) Coast-relative normalized wind profile averaged in time and distance from the coast
908 for all dual-Doppler profiles between 0000-1215 UTC. Positive distances from the coast
909 indicate increasing distance over water surfaces within the dual-Doppler domain. (b) As in
910 (a), but for the wind direction according to the color bar (in degrees from north).

911

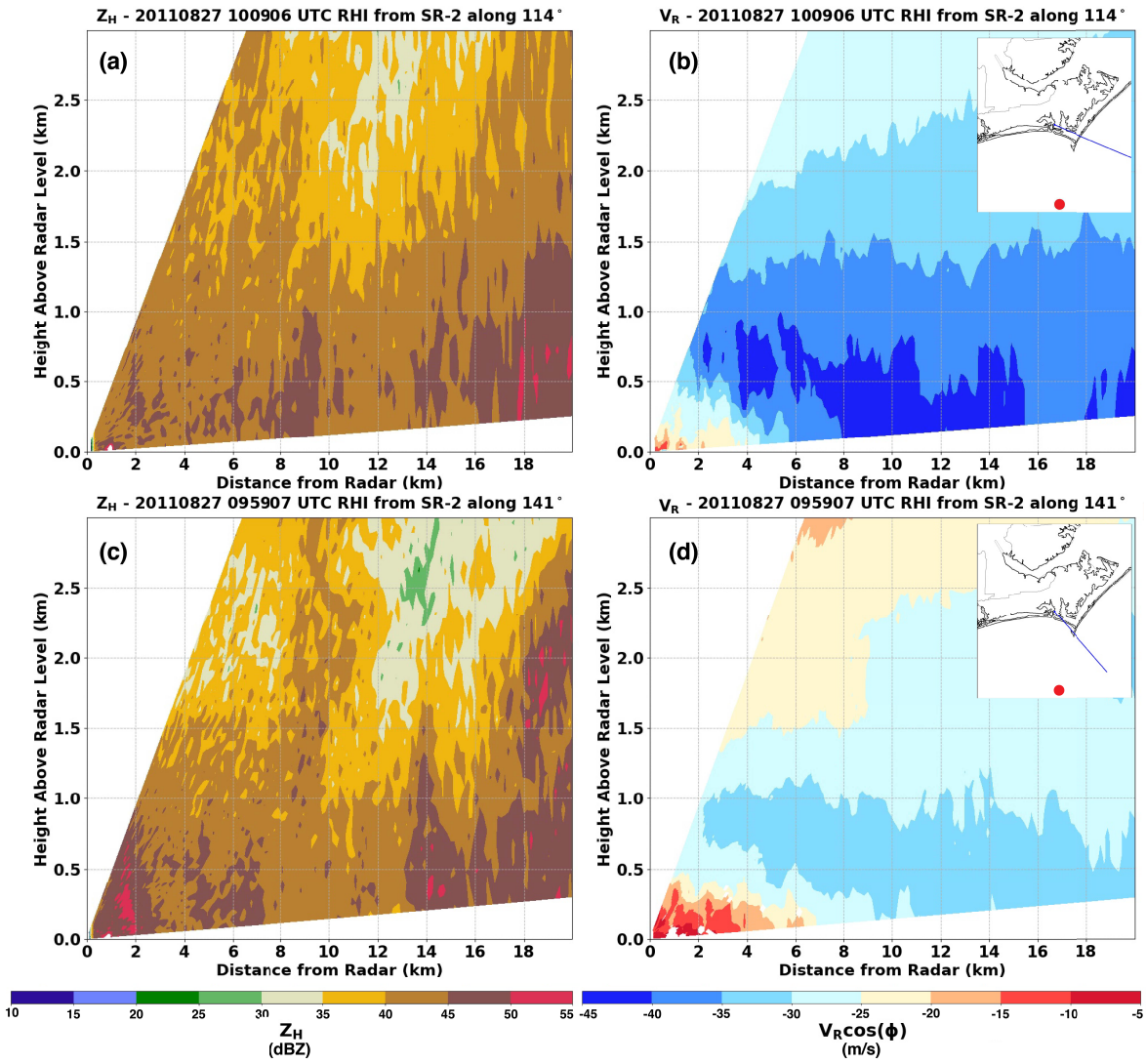

B78

B79 Figure 6. RHI from SMART radar 2 along an azimuth of (a, b) 114° from north at 1009 UTC and

B70 (c, d) 141° from north at 0959 UTC. (a, c) Radar radial velocity is shown projected into the

B7– horizontal according to the elevation along which it was taken. (b, d) A plan view of the

B7, RHI (blue line) and the 10 UTC location of Irene's center (red circle) overlain upon a map

B7K of the coastal region. It should be noted that at 1009 UTC (0959 UTC) the 8 km (6 km)

B7. range is approximately representative of the shoreline of the greater continental region and

B7B 18 km (8.5 km) is approximately the shoreline of the North Caroline barrier islands.

B86

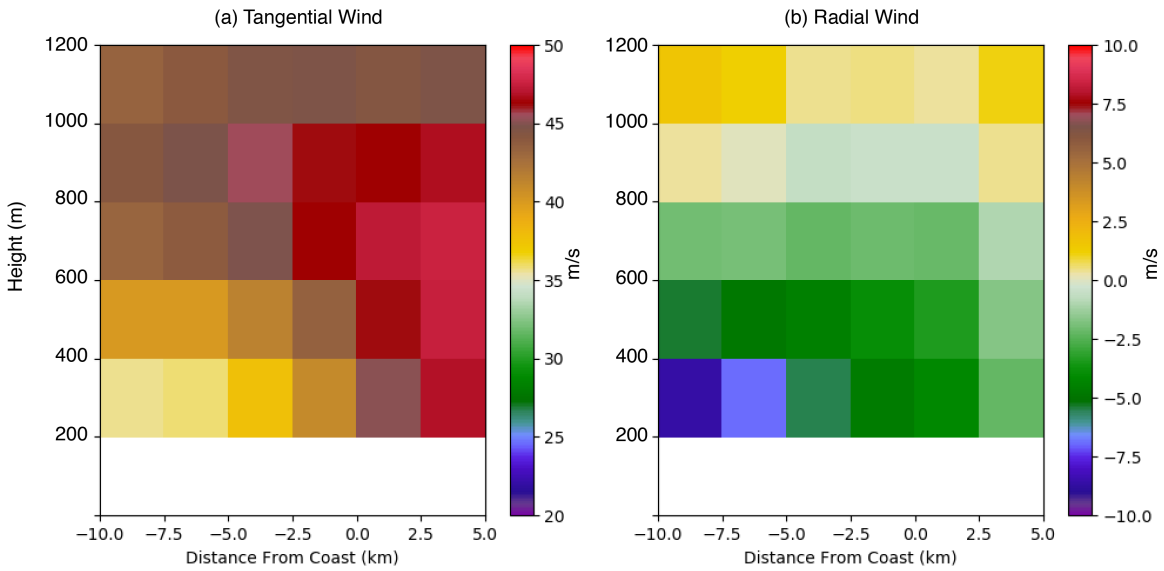

Figure 7. Full (not normalized) average coast-relative (a) tangential and (b) radial wind speeds ($m\ s^{-1}$) according to the color bars. Negative values indicate storm-relative inflow in (b).

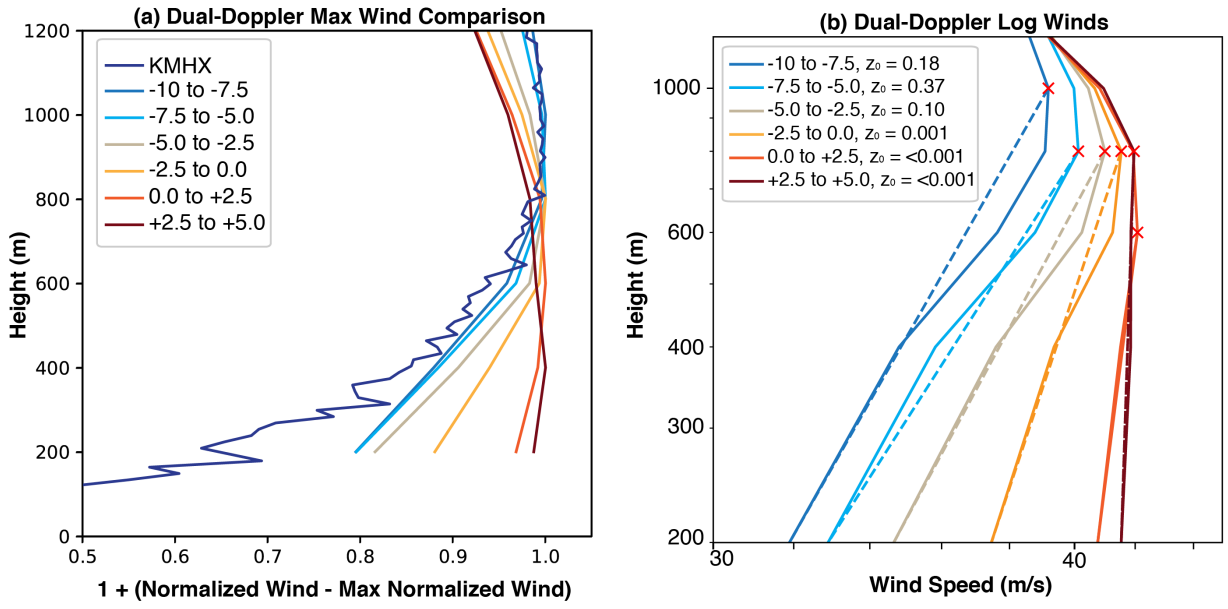

Figure 8. (a) A comparison of the coast-relative normalized boundary layer profiles from Figure 5 and an average boundary layer normalized profiles for VADs retrieved from KMHX. The coast relative distance is indicated according to the contour color in the inset legend. A

929 value of 1.0 indicates the maximum wind. (b) The mean boundary layer winds (full; solid
930 curves) compared to a logarithmic profile constructed between the maximum wind (red
931 crosses) and 200 m. The roughness length z_0 is shown in the legend and represents the value
932 required to maintain a log-linear profile between the maximum wind and the 200 m wind.
933

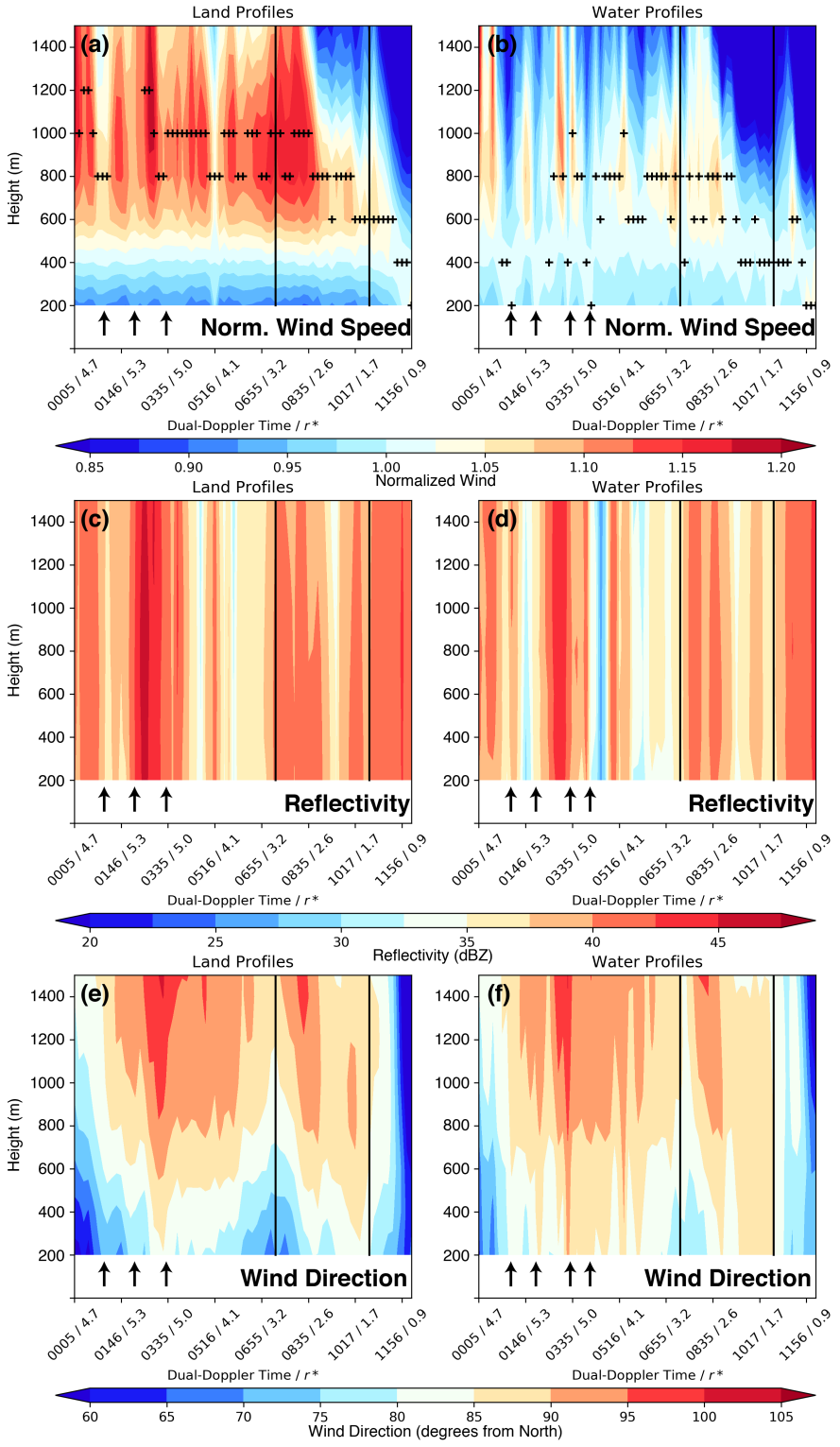

934

935 Figure 9. Normalized wind profiles (a) over land and (b) over water within the dual-Doppler

936 analysis domain subset shown in Figure 4. The labels along the x-axis indicate the dual-

937 Doppler time and the area-mean normalized-radius r^*. Profiles are constructed for each
938 dual-Doppler time (x-axis) in height (y-axis). The values of the normalized wind are shown
939 according to the colorbar at the bottom of the figure. The black lines indicate the separation
940 of the outer bands/inner core regime at $r^* = 3.0$ and the separation of the inner core/eyewall
941 regime at $r^* = 1.5$. The black +'s indicate the height of the maximum normalized wind. (c)
942 and (d) display land and water profiles of area-mean reflectivity, respectively. (e) and (f)
943 show the area-mean profiles of wind direction with height for land and water profiles,
944 respectively. The arrows in the figure depict periods of increased normalized winds in (a)
945 and (b), their corresponding periods of changing reflectivity in (c) and (d), and their
946 corresponding changes in wind direction in (e) and (f).
947

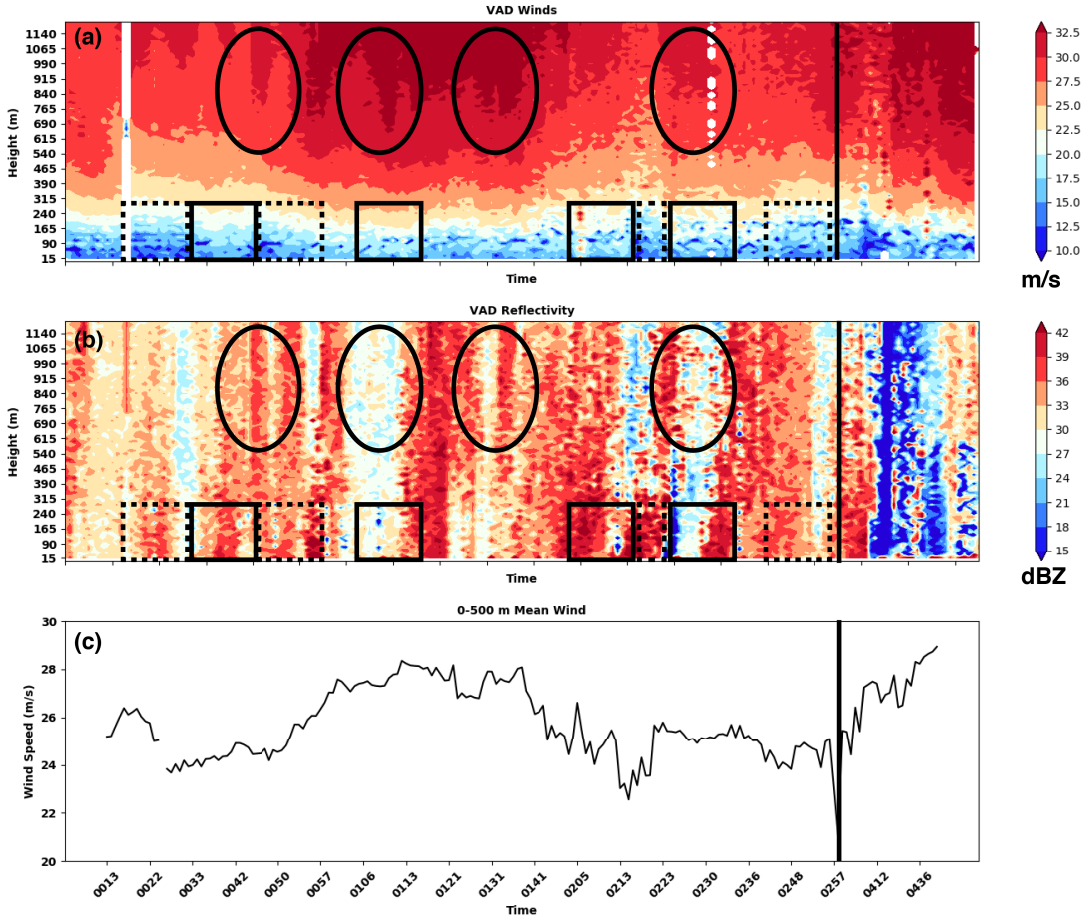

B0.

B0B Figure 10. Time series of RaXPol observed HBL structure from 0013 UTC to 0500 UTC. (a)

B–6 VAD-derived winds as a function of height (y-axis) over time (x-axis). Wind speeds (total)

B–7 are shown according to the colorbar to the right of (a). (b) As in (a), but for the vertical

B–8 profile of radar reflectivity. (c) The VAD-derived 0-500 m mean wind is shown for context.

B–9 In both (a) and (b), the black rectangles (dashed rectangles) indicate example periods during

B–0 which there are local wind maxima (minima) in the lower part of the VAD profiles. The

B— black ovals indicate periods of wind maxima in the upper part of the VAD profiles. The

B–, vertical black line denotes a temporal gap in RaXPol data.

B–K

B–.

B—B

B, 6

B, 7

B, 8

B, 9

B, 0

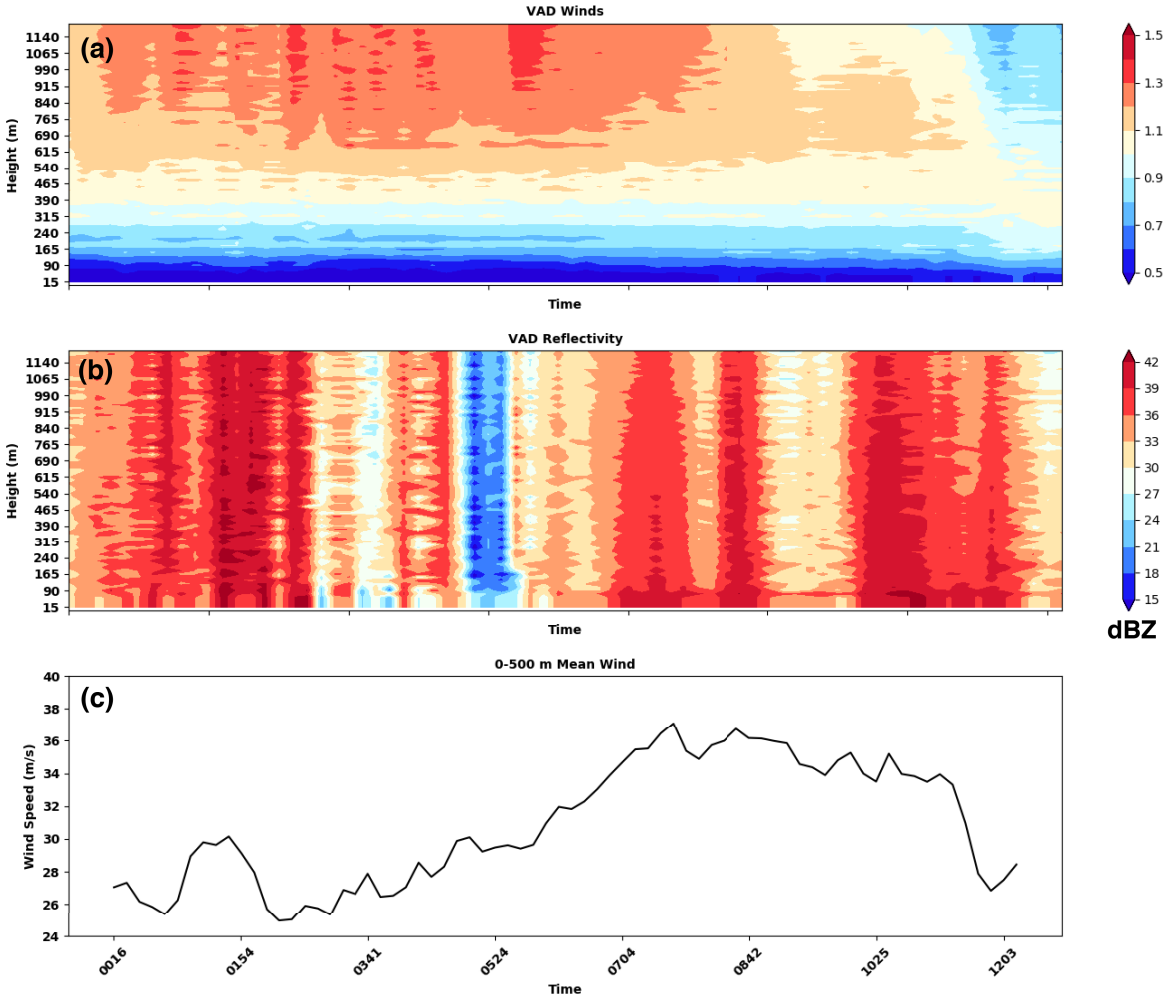

B, —

B, , Figure 11. Time series of KMHX VAD profiles as in Figure 10. (a) As in Figure 10a, but for the

B, K normalized wind.

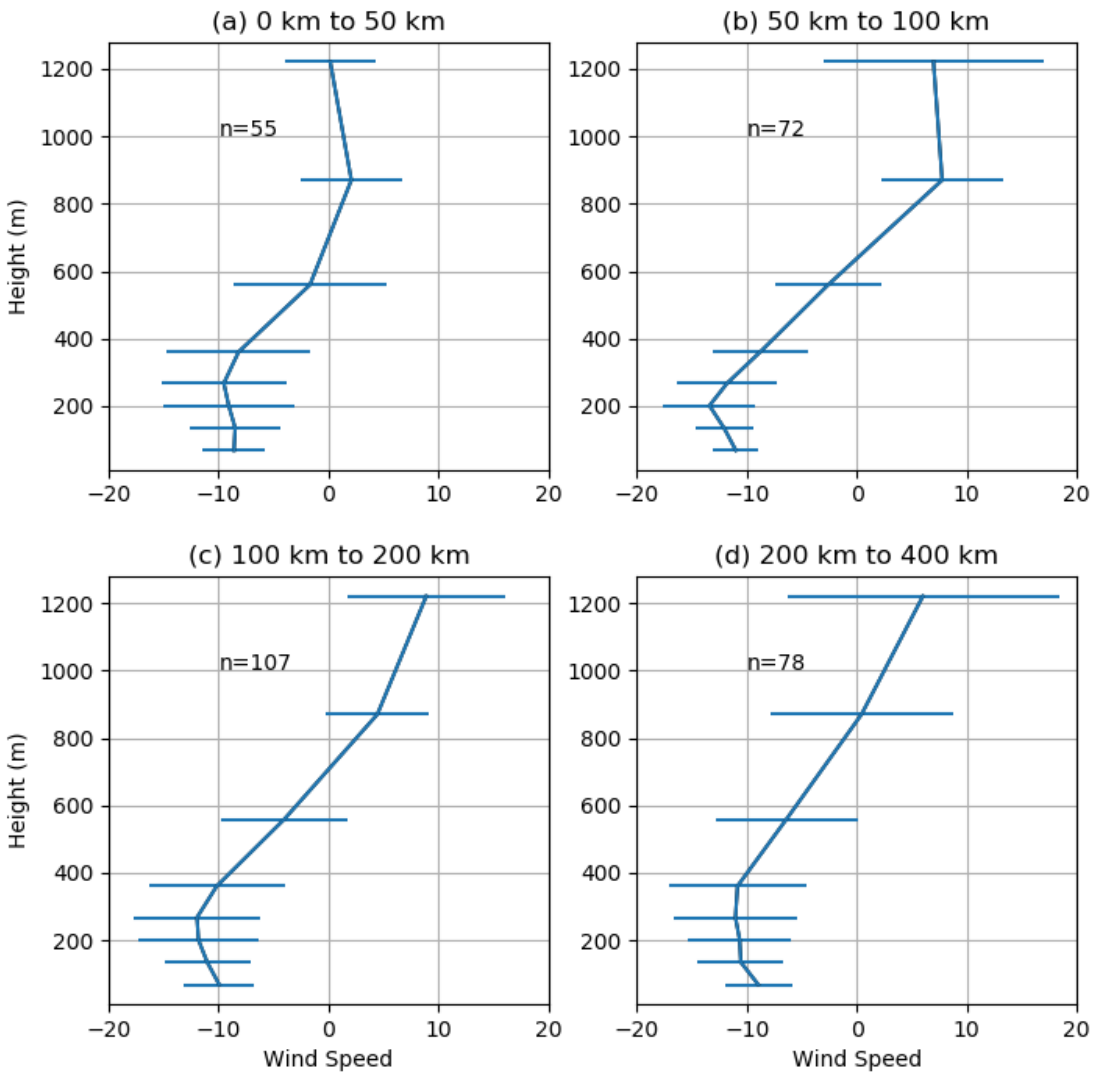

B, .

B, B Figure 12. Radial wind profiles derived from the KMHX VAD analysis. Profiles are shown (a)

BK6 0-50 km, (b) 50-100 km, (c) 100-200 km, and (d) 200-400 km from the center of circulation

BK7 of Irene. Wind speeds are shown in m s^{-1}.

BK8

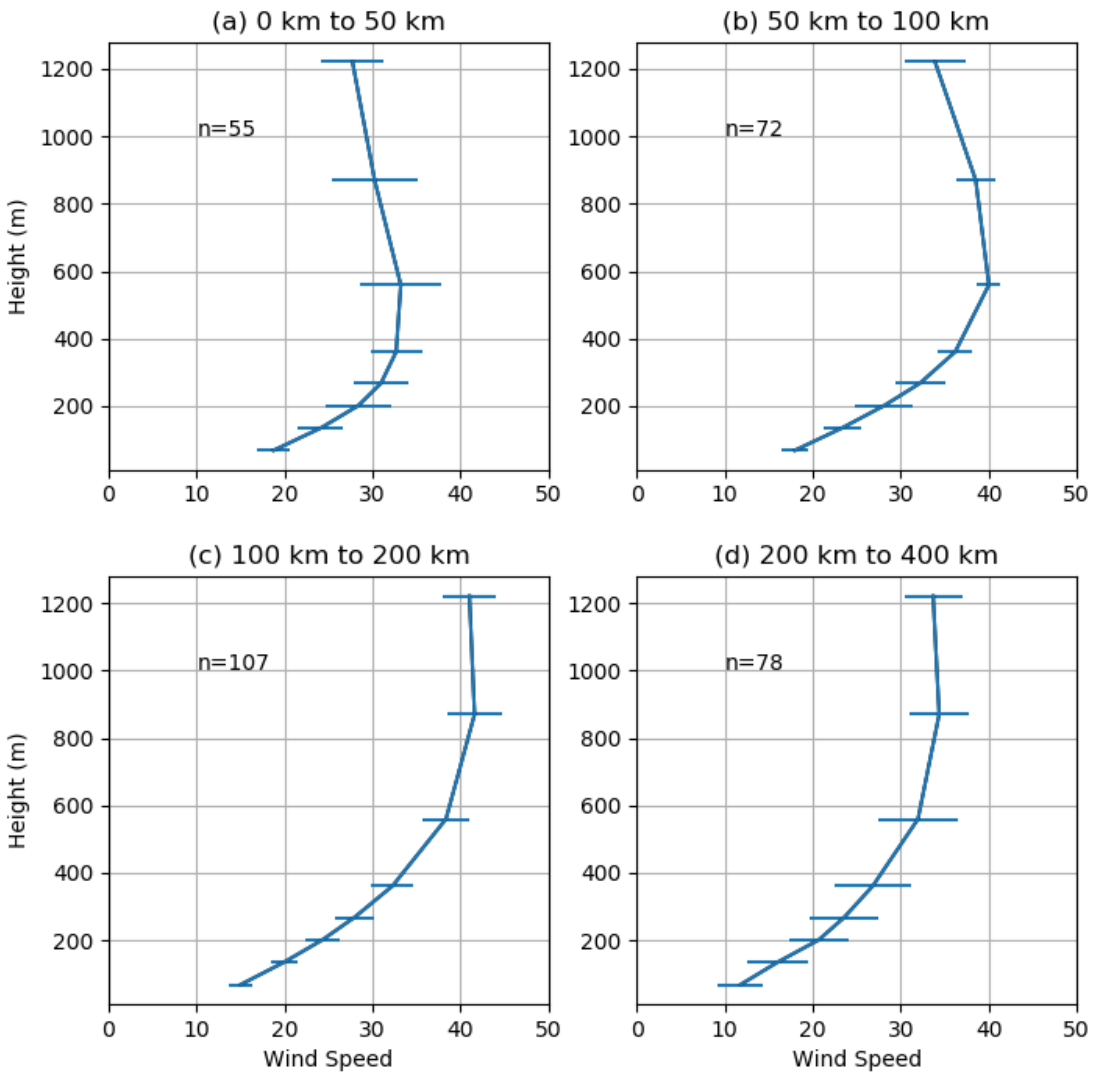

BK9

BK0 Figure 13. As in Figure 12, but for the tangential wind.

BK–

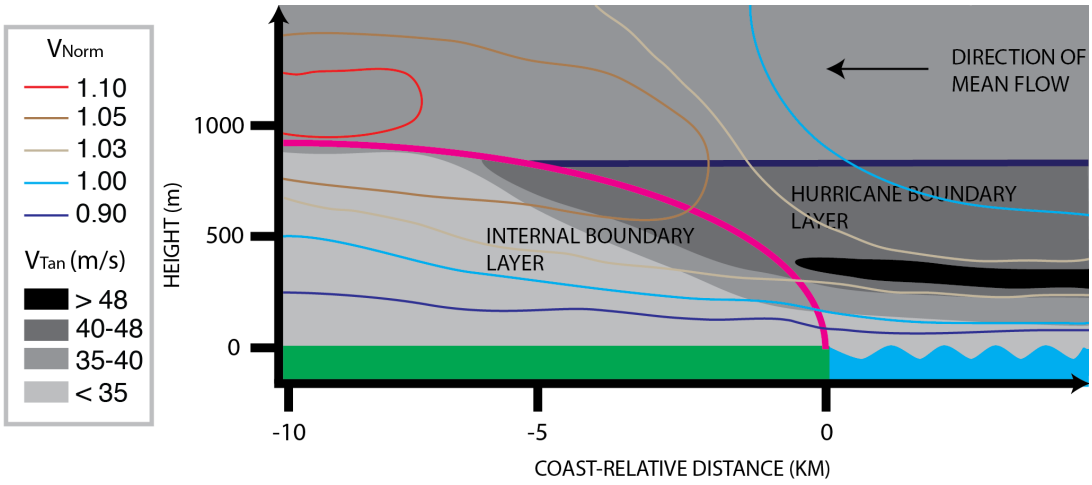

976

977 Figure 14. Conceptual model of the HBL transition across the coastal-interface for Hurricane
978 Irene. The dark blue line represents the height of the pre-existing HBL that results from
979 HBL dynamics over the open ocean. The magenta curve represents the growth of the
980 internal boundary layer response to the surface roughness discontinuity at the coast. The
981 tangential wind V_{tan} is shown via the color-filled contours according to the legend. The line
982 contours according to the legend indicate the approximate value of the mean state of the
983 coast-relative normalized wind V_{Norm}. In the figure the mean flow is directed from right to
984 left (toward coast).

985

986

987